Lens-free interferometric microscope for transparent materials

Roland A. Terborg

Thesis Advisor: Prof. Valerio Pruneri

PhD Thesis - 2018

A mis padres.

4

Abstract

As health systems fight against epidemics and infectious diseases, new forms of diagnostics need to be developed in order to meet the growing demand for services, often in locations without the necessary infrastructure. An emerging solution to this problem is point of care (POC) devices since they can provide rapid diagnostics without the need for specialized personnel or complex infrastructures.

In this thesis, we show the development of a POC platform for the rapid early detection of infection, in particular Sepsis, a whole-body inflammatory reaction with high mortality rates. The main components of this platform are: a lens-free interferometric microscope (LIM) and a microfluidic cartridge with a functionalized plasmonic chip for the label-free detection of biomarkers. The LIM is also able to measure the phase modulation in commercial plasmonic chips.

More specifically the thesis describes:

- The development of a LIM with a large field of view and depth of field showing a sensitivity of 1nm along the beam propagation axis, which allows, for instance, the measurements of ultra-thin (2nm thickness) transparent silica and protein monolayer microarrays.

- The generation of periodic structured light beams, obtained using a simple configuration including the birefringent elements of the LIM. These can be applied not only to imaging and biomarker detection but also in additive manufacturing and micro-structuring of surfaces.

- The phase measurement of commercial surface plasmon resonance chips for the detection of changes in the refractive index of liquids. The phase measurements provide a sensitivity for bulk refractive index changes that is about one order of magnitude larger than for intensity-based detection

under similar conditions. These results show a potential enhancement of the sensitivity of standard systems used in the biomedical community.

- The development of a POC device comprising the LIM as a reader of specifically designed plasmonic gold nanohole array chips. The reading of the phase signal in the LIM shows a sensitivity increased by one order of magnitude thanks to the enhanced localized surface plasmon resonance interaction. Low concentrations of proteins and bacteria (as low as a single unit) are detected in measurements that also include human samples. This platform has the potential to multiplex the signal for simultaneous detection of thousands or even millions of different biomarkers.

The LIM presented in this thesis is a very sensitive and robust imaging system with a high performance level for the detection of small quantities of transparent materials, with applications in microscopy and biomedicine.

Resumen

A medida que los sistemas de salud combaten epidemias y enfermedades infecciosas, nuevas formas de diagnóstico deben desarrollarse para satisfacer la creciente demanda de servicios, a menudo en lugares sin la infraestructura necesaria. Una solución emergente a este problema son los dispositivos de punto de atención (POC por sus siglas en inglés) ya que pueden proporcionar un diagnóstico rápido sin la necesidad de personal especializado o infraestructura compleja.

En esta tesis mostramos el desarrollo de una plataforma POC para la detección rápida y temprana de infecciones, en particular Sepsis, una reacción inflamatoria de todo el cuerpo con altas tasas de mortalidad. Los principales componentes de esta plataforma son: un microscopio interferométrico sin lentes (LIM por sus siglas en inglés) y un cartucho de microfluídica con un chip plasmónico funcionalizado para la detección de biomarcadores, libre de marcadores adicionales. El LIM es también capaz de medir la modulación de fase en chips plasmónicos comerciales.

Más específicamente, la tesis describe:

- El desarrollo del LIM con un gran campo de visión y profundidad de campo mostrando una sensibilidad de 1nm a lo largo del eje de propagación del haz, que permite, por ejemplo, las mediciones de microarreglos ultrafinos (grosor de 2nm) y transparentes de Sílica y de monocapas de proteína.

- La generación de haces de luz estructurados periódicos, obtenidos usando una configuración simple que incluye los elementos birrefringentes del LIM. Estos pueden ser aplicados no sólo a la detección de imágenes y biomarcadores, sino también a la fabricación aditiva y microestructuración de superficies.

- La medición de fase en chips comerciales por resonancia de plasmón super-

ficial para la detección de cambios en el índice de refracción de líquidos. Las mediciones de fase proporcionan una sensibilidad para cambios de índice de refracción en bulto que es aproximadamente un orden de magnitud mayor que para la detección basada en la intensidad con condiciones similares. Estos resultados muestran una potencial mejora de la sensibilidad de los sistemas estándar utilizados en la comunidad biomédica.

- El desarrollo de un dispositivo POC que comprende el LIM como lector de chips plasmónicos de oro con arreglos de nano-agujeros específicamente diseñados. La lectura de la señal de fase en el LIM muestra un aumento de un orden de magnitud en la sensibilidad gracias a la interacción mejorada por la resonancia de plasmón superficial localizado. Bajas concentraciones de proteínas y bacterias (tan bajas como una sola bacteria) se detectan en mediciones que también incluyen muestras humanas. Esta plataforma tiene el potencial de multiplexar la señal para la detección simultánea de miles o incluso millones de biomarcadores diferentes.

El LIM presentado en esta tesis es un sistema de imagen muy sensible y robusto con un alto nivel de rendimiento para la detección de pequeñas cantidades de materiales transparentes, con aplicaciones en microscopía y biomedicina.

Funding

Acknowledgements

The acknowledgements are probably one of the most difficult parts in a thesis, because it is for sure the section that is read the most, but it is nearly impossible to put in it everyone who actually deserves it. But even so, one has to try! In any case, thanks to you, reader, for actually opening this thesis!

Above all, I must thank my supervisor, Valerio Pruneri, since he made it possible for me to do my PhD in such an interesting project with all the necessary resources. I'm also very grateful to him for the time he has kindly dedicated to me, for everything that I have learned from him and, of course, for the funny moments during our meetings.

Thanks to Juan P. Torres for all the interesting discussions and for the support.
Thanks to the ones who have played an important role in my academic (and non-academic) development, especially in my former university, the UNAM. Therefore, lots of thanks to Karen Volke.

I also want to express my gratitude to Lluís and Dolors for making ICFO the way it is. Of course, they are not alone, I also would like to thank Anne, Alina, Núria, Silvia, Sol, Mery, Tomas,Niek, Rob, Jonas, Adri, Esther, Magda, Santi, María Jesús, César, Xavi, Juan, Chema, Carlos, José Carlos and all the people in the different units who have helped me and who make from ICFO an amazing place for research.

Thanks to the Opto group, big and indivisible (especially during lunch time!). They make you feel like being part of a big family that helps each other all the time.
A lot of thanks to Vittoria, Bruno, Alexandra, Dani, Vahagn, Rinu, Matej, Fe-

11

The LIM in a nutshell for the non-scientific reader

Microscopes are tools that help us see the small things that are invisible to the naked eye. There are several kinds of microscopes, each with different properties, allowing to see from cells in a section of tissue, to single molecules or even atoms.

An important part of a microscope is its image sensor and, over the last decades, there has been a significant advance in quality of these components. Even in our daily lives we can see how the cameras in our mobile phones have become better and better. They have reached a level of image quality such that by using simple add-ons that can be bought through on-line stores or even 3D-printed, a modern smartphone can be converted in an optical microscope that can be used for scientific purposes [1].

Optical microscopes with lenses can achieve a good spatial resolution allowing, for instance, to observe the small details from a cell. However, the price to pay for this resolution is that the field of view is proportionally narrowed down, this means, for high resolution it is only possible to see one cell at a time. But for some applications it is required to analyze large areas (several squared millimeters) of a sample, with enough resolution as to detect a kind of cells or bacteria within a section of tissue. A classical solution would be to scan the whole sample with a normal microscope, but this makes the analysis of large samples a cumbersome and slow task. This solution also adds more complexity to the instrument and usually increases the cost.

---

[1]See for example https://phys.org/news/2018-02-add-on-smartphone-fully-microscope.html

14

A counterintuitive but simple solution to the previous problem is to use the detector of a camera as it is, without any lenses. When we put an object between a light source (like a laser or an LED) and the detector, we are able to capture the shadow from this object with a resolution similar to the pixel size of the detector, which can be even smaller than 1μm. The advantage in this case is that additionally, in the same capture, we get all the other objects of interest that fit within the area of the detector.

If we capture an image of the object using LED or laser light, we might even see that this shadow becomes *wavy* due to the wave nature of light[2]. By using the appropriate computational algorithms, we can transform the blurry and wavy image into a sharp image of the object. The process of the image reconstruction from a diffracted image can be observed in Figure 2.6 (page 54).

Due to its simplicity and robustness, lens-free microscopy has been found to be a useful technology for the development of highly sensitive and inexpensive medical devices to detect, for example, cancerous cells[3]. However, medical applications where small quantities of proteins and other highly transparent materials need to be detected represent a bigger challenge. Solving this problem is the main objective of this thesis.

In this thesis, we have developed a lens-free interferometric microscope (LIM) that helps to detect protein layers that are as thin as a few nanometers. The LIM includes optical elements that affect the illumination beam according to its polarization[4] (see Figure 2.1 in page 47). These elements allow us to measure transparent samples through interference of light which, for this case, compares the propagation distance of two neighbour light rays, translating little differences in the height of a sample into differences in the intensity of the recorded image (see Figure 2.4 in page 51). After processing the images with our algorithms, we measure relative differences in the path of two beams that are as small as 1nm. This sensitivity allows us to detect, within less than 2 minutes, an array of dots with single layers of proteins, as well as the binding of the corresponding antibody (see Figure 2.11 in page 63).

In order to increase this sensitivity even more, we use *plasmonic* substrates.

---

[2]This phenomenon is called diffraction and it becomes stronger with large propagation distances.

[3]See www.photonics.com/Articles/Lens-Free_3-D_Microscope_Sharp_Enough_for/a57019

[4]The polarization of light refers to the direction of oscillation of the electric field of the light.

One of these substrates is made of a thin layer of gold with an array of holes with dimensions in the order of hundreds of nanometers (see Figure 3.1d) in page 70), specially designed to interact with the incoming light in a way that only specific wavelengths[5] are allowed to be transmitted. This behavior is affected by the properties of the material that is deposited on top of the plasmonic substrate. The different regions of the plasmonic substrate are treated in different ways, such that each region is sensitive to different proteins, bacteria and other biomaterials. A change in the transmitted light in a given position of the chip is directly related to the presence of this biomaterial in the medium to be analyzed. Moreover the plasmonic chip interacts with the transmitted light in a way that the corresponding signal is amplified about 10 times, allowing to quantify the deposition of small quantities of biological material, like proteins and cells, in small volumes of liquid.

Due to its high sensitivity, the LIM constitutes the optical reader of the sensing platform of the RAIS project (see the section *Sepsis and the EU project RAIS* in page 26), enabling the detection of low quantities of different proteins and single Escherichia coli bacteria.
This technology has the potential to detect simultaneously from thousands to millions of different biomaterials and, in a near future, could lead to a portable medical platform that provides fast diagnosis of Sepsis and many other diseases.

---

[5]The wavelength is a property of light related to the frequency of oscillation of its electromagnetic field. In the visible part of the spectrum, the wavelength is related to the color of the light that we see.

16

El LIM resumido para el lector no científico

Los microscopios son herramientas que nos ayudan a ver las pequeñas cosas que son invisibles a simple vista. Existen varios tipos de microscopios, cada uno con diferentes propiedades, que permiten ver desde las células de una sección de tejido hasta moléculas individuales o incluso átomos.

Una parte importante de un microscopio es su sensor de imagen y, en las últimas décadas, ha habido un avance significativo en la calidad de estos componentes. Incluso en nuestra vida cotidiana podemos ver cómo las cámaras de nuestros teléfonos móviles se han vuelto cada vez mejores. Han alcanzado un nivel de calidad de imagen tal que mediante el uso de complementos simples que se pueden comprar a través de tiendas en línea o incluso imprimir en 3D, un teléfono moderno se puede convertir en un microscopio óptico que se puede utilizar con fines científicos [6].

Los microscopios ópticos con lentes pueden lograr una buena resolución espacial, lo que permite observar, por ejemplo, los pequeños detalles de una célula. Sin embargo, el precio a pagar por esta resolución es que el campo de visión se reducirá proporcionalmente, es decir, con una resolución alta sólo es posible ver una célula a la vez. Pero para algunas aplicaciones, se requiere analizar grandes áreas (varios milímetros cuadrados) de una muestra, con suficiente resolución como para detectar un tipo de células o bacterias dentro de una sección de tejido. Una solución clásica sería escanear toda la muestra con un microscopio normal, pero esto hace que el análisis de muestras grandes sea una tarea tediosa y lenta. Esta solución también agrega más complejidad al instrumento y generalmente

---

[6]Ver por ejemplo https://phys.org/news/2018-02-add-on-smartphone-fully-microscope.html

aumenta su costo.

Una solución contraintuitiva pero simple al problema anterior es usar el detector de una cámara tal cual, sin ningún tipo de lentes. Cuando colocamos un objeto entre una fuente de luz (como un láser o un LED) y el detector, podemos capturar la sombra de este objeto con una resolución similar al tamaño de píxel del detector, que puede ser incluso menor que 1 μm. La ventaja en este caso es que, además, en la misma captura obtenemos todos los demás objetos de interés que quepan dentro del área del detector.
Si capturamos una imagen del objeto usando luz de un LED o de un láser, incluso podríamos ver que esta sombra es *ondulada*, debido a la naturaleza ondulatoria de la luz [7]. Al usar los algoritmos computacionales apropiados, podemos transformar la imagen borrosa y ondulada en una imagen nítida del objeto. El proceso de reconstrucción de imágenes a partir de una imagen difractada se puede observar en la figura 2.6 (página 54).

Debido a su simplicidad y robustez, se ha descubierto que la microscopía sin lentes es una tecnología útil para el desarrollo de dispositivos médicos portátiles que son altamente sensibles y de bajo costo, por ejemplo para la detección de células cancerosas [8]. Sin embargo, las aplicaciones médicas que necesitan la detección de pequeñas cantidades de proteínas y otros materiales altamente transparentes, representan un desafío mayor y resolver este problema es el principal objetivo de esta tesis.

En esta tesis hemos desarrollado un microscopio interferométrico sin lentes (LIM) que ayuda a detectar capas de proteínas que son tan delgadas como unos pocos nanómetros. El LIM incluye elementos ópticos que afectan al haz de iluminación según su polarización [9] (ver la Figura 2.1 en la página 47). Estos elementos nos permiten medir muestras transparentes mediante la interferencia de la luz que, en este caso, compara la distancia de propagación de dos rayos de luz vecinos, traduciendo pequeñas diferencias en la altura de una muestra en diferencias de intensidad en la imagen grabada (ver la Figura 2.4 en la página 51). Después de procesar las imágenes con nuestros algoritmos, medimos las diferencias relativas en el camino de dos haces que son tan pequeñas como 1nm.

---

[7] Este fenómeno se llama difracción y se hace más fuerte con grandes distancias de propagación .

[8] Ver www.photonics.com/Articles/Lens-Free_3-D_Microscope_Sharp_Enough_for/a57019

[9] La polarización de la luz se refiere a la dirección de oscilación del campo eléctrico de la luz.

Esta sensibilidad nos permite detectar, en menos de 2 minutos, una matriz de puntos con capas individuales de proteínas, así como la unión del anticuerpo correspondiente (ver la Figura 2.11 en la página 63).

Para aumentar aún más esta sensibilidad, utilizamos sustratos *plasmónicos*. Uno de estos sustratos está hecho de una fina capa de oro con una serie de orificios con dimensiones del orden de cientos de nanómetros (ver Figura 3.1d) en la página 70), especialmente diseñado para interactuar con la luz entrante de una manera que sólo longitudes de onda específicas [10] pueden transmitirse. Este comportamiento se ve afectado por las propiedades del material que se deposita sobre el sustrato plasmónico. Las diferentes regiones del sustrato plasmónico se tratan de diferentes maneras, de modo que cada región es sensible a diferentes proteínas, bacterias y otros biomateriales. Un cambio en la luz transmitida en una posición dada del chip está directamente relacionado con la presencia de este biomaterial en el medio a analizar. Además, el chip plasmónico interactúa con la luz transmitida de forma que la señal correspondiente se amplifica aproximadamente 10 veces, lo que permite cuantificar la deposición de pequeñas cantidades de material biológico, como proteínas y células, en pequeños volúmenes de líquido.

Debido a su alta sensibilidad, el LIM constituye el lector óptico de la plataforma de detección del proyecto RAIS (ver la sección *Sepsis and the EU project RAIS* en la página 26), permitiendo así la detección de pequeñas cantidades de diferentes proteínas y bacterias individuales de Escherichia coli.
Esta tecnología tiene el potencial de detectar de forma simultánea desde miles hasta millones de diferentes biomateriales y, en un futuro cercano, podría conducir a una plataforma médica portátil que proporcione un diagnóstico rápido de Sepsis y de muchas otras enfermedades.

---

[10]La longitud de onda es una propiedad de la luz relacionada con la frecuencia de oscilación de su campo electromagnético. En la parte visible del espectro, la longitud de onda está relacionada con el color de la luz que vemos.

List of publications included in this thesis

Journal articles

- Roland A. Terborg, Josselin Pello, Ilaria Mannelli, Juan P. Torres, and Valerio Pruneri. **Ultrasensitive interferometric on-chip microscopy of transparent objects**. Science Advances, 2(6), 2016.

- Filiz Yesilkoy, Roland A. Terborg, Josselin Pello, Alexander A. Belushkin, Yasaman Jahani, Valerio Pruneri, and Hatice Altug. **Phase-sensitive plasmonic biosensor using a portable and large field-of-view interferometric microarray imager**. Light: Science & Applications, 7(2):17152, 2018.

Journal articles in review process

- Roland A. Terborg,Juan P. Torres, and Valerio Pruneri. **A technique for generating periodic structured light beams using birefringent elements**.

- Priyanka Dey, Nuria Fabri, Olalla Calvo, Roland A. Terborg, Alexander Belushkin, Filiz Yesilkoy, Anna Fàbrega, Juan Carlos Ruiz-Rodriguez, Juan José González-López, M.-Carmen Estevez, Hatice Altug, Valerio Pruneri and Laura Lechuga. **Label-free bacteria quantification in blood plasma by a bioprinted microarray based interferometric point-of-care device**.

Patents

- Valerio Pruneri, Roland A. Terborg, Josselin Pello, Marc Jofre, Pedro Martínez. **Aparato para explorar una propiedad óptica de una muestra**. Filed patent application , 2018.

Relevant Presentations

- Roland A. Terborg, Josselin Pello, Ilaria Mannelli, Juan P. Torres, and Valerio Pruneri. **Multispectral Interferometric On-Chip Microscopy for Biosensing**. 2017 Conference on Lasers and Electro-Optics Europe & European Quantum Electronics Conference (CLEO/Europe-EQEC), Munich, Germany, 2017. (Oral presentation)

- Roland A. Terborg. **RAIS project: Interferometric microscopy technology**. Photonics for Health, Poseidon Summer School 2017, San Martino di Castrozza, Italy, 2017. (Invited Talk)

- Roland A. Terborg. **Portable lens-free microscopy with sub-nanometric depth sensitivity for thin films and protein detection**. International School on Computational Microscopy (ISCM), Amalfi, Italy, 2017. (Poster / 1st Prize to the best poster)

Contents

Introduction

Microscopy, global health issues and point of care devices

The invention of the optical microscope has changed the way we understand the world on the small scale. By opening the window to the microscopic world, we have learned how our health can be put to risk by diverse 'invisible' pathogens, and has given us a better image of the inner processes of our cells, therefore allowing us to find ways to prevent or correct their malfunctioning.

Microscopy is now an interdisciplinary tool, which has been constantly expanding and evolving, for instance, in its optical branch there are already a myriad of different techniques. Some of these rely on highly precise optical equipment and special illumination in order to achieve a spatial resolution that goes beyond the classical diffraction limit [1,2], whereas others rely less on physical elements and more on computational algorithms, being able to avoid the use of lenses and still obtain enough resolution for single cell imaging [3].

A good example of the importance of microscopy can be found in clinical laboratories, where standard light microscopes can save lives by helping to detect malaria, tuberculosis and other diseases. Despite the fact that the analyses can be carried out without cutting edge microscopes, there are still many regions around the globe where these laboratory tests cannot be performed. A mass-scale production of these microscopes would not be enough to solve the global health problem of providing proper diagnostics, however, since these clinical analyses also require trained personnel, sample treatments and specialized facilities. This slows down the delivery of the diagnostics, increases the costs of the analysis and limits these services to zones with the necessary infrastructure [4]. Therefore, expanding the reach of health services around the world (with a special focus on developing countries) is one of the main objectives in global

health policies, and it is being supported by an increase in funding at international level [5]. Because of the constraints that are being faced, the medical and scientific communities are changing the paradigm for diagnostics, going from laboratory analyses to point of care (POC) tests, which are less limiting and, in many cases, the process is automatized, faster and less expensive [6–8].

POC platforms are generally required to detect small quantities of biomaterial, such as bacteria, antibodies, nucleic acids, etc. [8], and, therefore, one of the main challenges they face is to achieve the necessary sensitivity without complex processes or bulky laboratory equipment. Signal multiplexing, allowing for simultaneous detection of several pathogens and disease biomarkers, can be desirable as well, in order to reduce time and costs. To meet these requirements, new POC devices often adopt the label-free and lab-on-a-chip format for which nanophotonics, microfluidics, microarrays and microscopy are some of the preferred technologies [8].

Several platforms aimed at the development of compact imaging-based POC devices have been proposed, with some of them exploiting the high quality images from cameras in commercial mobile phones [9, 10]. Lens-free microscopy has also emerged as a technology that is well-suited for this kind of applications, since it reduces costs from optical elements and space, while providing a large field of view that eliminates mechanical scanning parts [11].

Thus far, the reported sensitivity of lens-free microscopes has not been sufficient for the detection of small biomarkers and proteins without resorting to additional signal enhancement techniques, like plasmonic substrates [12]. This lack of sensitivity is a technical challenge that, if solved, opens the path to new applications of lens-free microscopes.

Sepsis and the EU project RAIS

Sepsis is among the diseases that have recently been gaining more attention, due to its economic impact and high mortality rate.

"Sepsis is a potentially fatal whole-body inflammatory reaction caused by severe infection and, with a mortality rate of 35%, is responsible for ∼20,000 deaths per day worldwide. The cost of Sepsis is high and rising. In 2008, > €10 billion was spent on hospitalizations for Sepsis in both Europe and USA." [13]

A rapid detection of Sepsis increases the survival rate for patients, but laboratory analysis usually takes several hours, if not days.

Commercial systems like ALERE (Abbott) and LABGEO (SAMSUNG) can
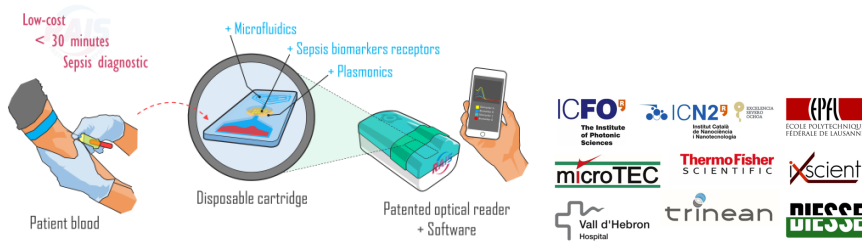
Figure 1: The RAIS concept and involved partners. Image taken from [13].

provide fast detection for some of the biomarkers that are associated with Sepsis. However, these systems do not show multiplexation capabilities, which are necessary for a fast and full diagnostics of Sepsis and its cause.

The overall objective of the RAIS project (www.rais-project.eu) was to develop a label-free POC platform that is able to detect several Sepsis biomarkers in human blood, using microarray technology. The analysis needs to be performed in 30 minutes using disposable microfluidic cartridges (see Figure 1).

In order to meet the required high sensitivity, the proposed detection scheme involves specifically designed plasmonic chips with sharp phase responses that are read by a novel interferometric reader, which is a compact lens-free microscope with a large field of view and depth of field, allowing larger microarrays and, therefore, more biomarkers to be simultaneously detected.

Aim of this thesis

The main aim of this thesis is the development of the optical reader of the POC device for the RAIS project, the novel lens-free interferometric microscope (LIM). Specific objectives include:

- Development of the LIM and the necessary computational algorithms for the detection of protein monolayers and transparent microarrays with thicknesses of the order of 1nm.

- Integration of the LIM into a POC platform and detection of small concentrations of proteins exploiting the phase signal enhanced by plasmonic gold nanohole array substrates.

- Exploitation of the sharp phase response in commercial surface plasmon resonance chips for an enhanced detection of refractive index changes.

Outline of the Thesis

Chapter 1

The Savart plates, i.e. a proper combination of birefringent elements, are the key optical components of the LIM, and their effects on polarized light are presented in this chapter. In particular, it is shown how these elements can be used to shape Gaussian beams, with curved wavefronts, into several types of structured light beams, which may be potentially suitable for imaging or targeted illumination of microarrays. Applications towards additive manufacturing and surface micro-structuring are also explored.

Chapter 2

The configuration of the LIM and its optical response are explained, together with the phase-shifting interferometry technique and the image reconstruction algorithms. Detection of ultra-thin transparent samples and protein monolayers, with thicknesses of only few nanometers, is demonstrated.

Chapter 3

The POC version of the LIM, for the measurement of microfluidic cartridges, is presented. The sensitivity of the LIM is enhanced by the large phase response of the specifically designed plasmonic chips that are in the cartridges. The performance of the platform for the detection of biomarkers is analyzed.

Chapter 4

Small changes in the refractive index of liquids are measured with the LIM and a commercial surface plasmon resonance prism. The sensitivity enhancements of the LIM due to the use of the commercial plasmonic chips, and vice versa, are analyzed. The results suggest that the LIM could improve the already highly sensitive commercial systems used in biomedical and pharmaceutical fields.

Chapter 1

Structured light through birefringence

1.1 Abstract

A simple technique is presented for shaping a Gaussian beam with curved wavefronts to produce scalable periodic intensity patterns of the form $\cos^{2n}(k_x x) \cos^{2m}(k_y y)$, among many others. We demonstrate how to generate them experimentally by using only a combination of birefringent crystals known as Savart plates and linear polarizers. Applications for photolithography, micro-lens array fabrication and 3D printing are proposed.

1.2 Introduction

Periodically structured light patterns play an important role in imaging technologies, from 3D imaging of microscopic and macroscopic objects [14], enabling biometric recognition in commercial mobile devices [15], to pushing the spatial resolution beyond the diffraction limit [1] [16]. For some applications it is necessary to be able to control and to modify illumination properties like position, periodicity and wavelength. Spatial light modulators (SLMs) based on microelectromechanical systems and liquid crystal arrays are the most common instruments used for this task. A more simple approach can be derived from Young's double pinhole experiment, which generates intensity patterns in

the form of cos^2. In fact, by using a pinhole mask, it is possible to generate different kinds of illumination patterns [17]. Although versatile, SLMs can be expensive and in some cases their pixelated nature will deteriorate the quality of the resulting beam. Additionally, most of these devices are not suitable for high power applications. Pinhole masks, on the other hand, may deliver a precise and smooth pattern, but they will not be dynamic and will have a very low efficiency.

In this work, we introduce a technique that can generate several kinds of periodical patterns by using passive and inexpensive optical components such as linear polarizers and Savart plates. These have proven to be ideal elements for producing interference even with low-coherence light [18] as well as being suitable for integration into a single compact device and for use with high-energy sources.
The presented technique provides a wide variety of regular and scalable patterns, for example in the form of $cos^{2n}(k_x x + \alpha_x)cos^{2m}(k_y y + \alpha_y)$. We also show, as a proof of concept, how these beams could be implemented for micro-structuring surfaces.

1.3   The Savart Plate

A Savart plate (SP) is an optical element composed of two identical birefringent crystals (for example Calcite, Quartz, alpha-BBO) cemented together, each with their optical axes at $45°$ to the surface normal and rotated through $90°$ with respect to each other. This element works in a similar way to a polarizing beam splitter where the two orthogonally polarized beams travel parallel to each other, but with a lateral displacement S, as depicted in Figure 1.1.

The optical axis of the first birefringent crystal of the SP lies in the horizontal plane (xz) just like the polarization vector of the horizontally polarized beam. Due to the angle between the optical axis and the beam, extraordinary refraction in the xz plane is produced. On the other hand, the vertically polarized beam shows normal incidence to the crystal and since its polarization vector is orthogonal to the optical axis it does not experience refraction [19]. For the second birefringent crystal, the optical axis lies in the vertical plane (yz). Therefore, the horizontally polarized beam is now an ordinary beam that continues propagating along z while the vertically polarized beam experiences extraordinary refraction in the yz plane. At the output of the SP, both beams propagate along z but are sheared by a distance S, which depends on the bire-fringence properties, the thickness of the crystals and on the wavelength of the
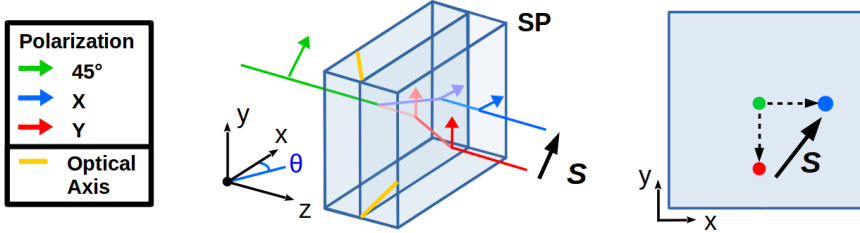
Figure 1.1: Splitting process of a linearly polarized beam into two parallel beams with orthogonal polarization and a lateral displacement S, using a Savart plate (SP).

light [18]. A tilt in the SP will lead to a change in the angle of incidence of the input beam and to a difference in the relative phase between the ordinary and extraordinary components [20–24]. Following equation 1 in [21], if the SP is tilted by a very small angle θ contained in the plane xz, as in Figure 1.1, then the relative phase difference α between both rays becomes

$$\alpha \propto \frac{2\pi}{\lambda} t [\frac{n_o^2 - n_e^2}{n_o^2 + n_e^2} \theta], \tag{1.1}$$

here λ is the wavelength of the beam, t is the thickness of the SP and n_o and n_e are the ordinary and extraordinary refractive indices of the crystals, respectively. We have experimentally confirmed that phase differences for visible light in a range larger than $-2\pi \leq \phi_0 \leq 2\pi$ can be introduced without producing any important side effects such as changes in beam separation or displacement, since they are typically smaller than the pixel size of our detectors. In the same way we have been able to verify that for small tilting angles of our SP (smaller than 2°) we obtain a linear behavior in α [18].

1.4 Analytical description

When a linearly polarized and uniform plane wave enters a SP, this element will act merely as a variable retarder. This follows from the fact that any transverse displacement results in a beam that is equivalent to the original, except for the induced relative phase delay between the two polarization components. However, when the input beam has a curved wavefront, for example a Gaussian

beam a long distance from the waist, by placing a combination of polarizers and SPs we are able to get different intensity modulations.

To explain how these patterns are generated, we start from the expression of the electric field of a Gaussian beam in the paraxial approximation

$$E = E_0 \frac{w_0}{w(z)} \exp\left(-\frac{r^2}{w^2(z)} + i\frac{kr^2}{2R(z)} - i\tan^{-1}\frac{z}{z_R}\right) \tag{1.2}$$

where E_0 is the amplitude of the electric field at the beam waist, $z_R = kw_0^2/2$ is the Rayleigh range, $k = 2\pi/\lambda$, $r^2 = x^2 + y^2$,

$$w(z) = w_0\sqrt{1 + \left(\frac{z}{z_R}\right)^2} \tag{1.3}$$

is the beam radius at position z and

$$R(z) = z\sqrt{1 + \left(\frac{z_R}{z}\right)^2} \tag{1.4}$$

is the curvature of the beam. The term $\tan^{-1} z/z_R$ is the Gouy phase shift. We are interested in the beams at a long distance from the beam waist ($z \gg z_R$), where the curvature becomes important. In this case, $w(z) \sim w_0 z/z_R$ and $R(z) \sim z$, so that

$$E \approx E_G = \frac{z_R E_0}{z} \exp\left[-\left(\frac{z_R}{w_0 z}\right)^2 r^2 + i\gamma r^2 - i\tan^{-1}\frac{z}{z_R}\right], \tag{1.5}$$

where

$$\gamma = \frac{\pi}{\lambda z} \tag{1.6}$$

and the corresponding intensity profile will, therefore, be

$$I_G = \frac{z_R^2 |E_0|^2}{z^2} \exp\left[-2\left(\frac{z_R}{w_0 z}\right)^2 r^2\right]. \tag{1.7}$$

As the linearly polarized beam traverses the SP, two copies of the input beam are generated, with orthogonal polarizations, and displaced by the shear distance S. By appropriately tilting the SP, the beams can show a phase difference α. After the SP, a polarizer projects the polarization of the two output beams into a common polarization. The vector that connects any two split points is given

by $\mathbf{S} = S_x \hat{x} + S_y \hat{y}$. Assuming that the separation between beams $S = \sqrt{S_x^2 + S_y^2}$ is much smaller than the beam size $(w_0 z/z_R)$, and that the beam amplitudes are equally split by the SP and are equally projected to the polarizer's transmission axis, then the output beam reads

$$
E_{out} = \frac{1}{2} \frac{z_R E_0}{z} \exp \left[- \left(\frac{z_R}{w_0 z} \right)^2 r^2 - i \tan^{-1} \frac{z}{z_R} \right] \times
$$
$$
\left\{ \exp \left[i\gamma \left(x - \frac{S_x}{2} \right)^2 + i\gamma \left(y - \frac{S_y}{2} \right)^2 - i\frac{\alpha}{2} \right] + \right. \tag{1.8}
$$
$$
\left. \exp \left[i\gamma \left(x + \frac{S_x}{2} \right)^2 + i\gamma \left(y + \frac{S_y}{2} \right)^2 + i\frac{\alpha}{2} \right] \right\}.
$$

Using eq. 1.5, the outcoming field can be written as

$$
E_{out} = \frac{E_G}{2} \exp \left[i\gamma \left(\frac{S_x^2}{4} + \frac{S_y^2}{4} \right) \right] \left\{ \exp \left[-i\gamma \left(xS_x + yS_y \right) - i\frac{\alpha}{2} \right] + \right.
$$
$$
\left. \exp \left[i\gamma \left(xS_x + yS_y \right) + i\frac{\alpha}{2} \right] \right\} \tag{1.9}
$$

$$
E_{out} = E_G \exp \left[i\gamma \left(\frac{S_x^2}{4} + \frac{S_y^2}{4} \right) \right] \cos \left(\gamma \, \mathbf{S} \cdot \mathbf{r} + \frac{\alpha}{2} \right). \tag{1.10}
$$

The intensity of the output beam is written as

$$
I_{out} = I_G \cos^2 \left(\gamma \, \mathbf{S} \cdot \mathbf{r} + \frac{\alpha}{2} \right). \tag{1.11}
$$

The effect of the SP and linear polarizer on a linearly polarized Gaussian beam with a large curvature is to produce a structured light beam with the original Gaussian intensity profile but modulated by a $\cos^2$ pattern. Note that by controlling the phase difference α we can gradually change from a $\cos^2$ to a $\sin^2$ pattern. The same result can be achieved in a controlled way by rotating one of the polarizers by 90°, as this changes the sign of the polarization projection.

We can combine several SPs and polarizers, with independent orientations, separation distances and phase shifts, to generate quite arbitrary patterns of light. For instance, we may have a linear polarizer (P1), followed by a Savart plate (SP1) and a linear polarizer (P2), all oriented along $\hat{x}$, generating two

beams with a separation S_x and a phase difference α_1. A second Savart plate (SP2) is oriented along $\hat{y}$ followed by a linear polarizer (P3) oriented along $\hat{x}$, generating two beams separated by a distance S_y with a phase difference α_2. After SP1 and P2, the field in eq. 1.10 is written as

$$E_{out_1} = E_G \exp\left(i\gamma \frac{S_x^2}{4}\right) \cos\left(\gamma S_x x + \frac{\alpha_1}{2}\right). \tag{1.12}$$

The splitting process of SP2 will only affect the y coordinate, so that, after P3:

$$E_{out_2} = E_G \exp\left[i\gamma\left(\frac{S_x^2}{4} + \frac{S_y^2}{4}\right)\right] \cos\left(\gamma S_x x + \frac{\alpha_1}{2}\right) \cos\left(\gamma S_y y + \frac{\alpha_2}{2}\right) \tag{1.13}$$

with a resulting intensity pattern

$$I_{out_2} = I_G \cos^2\left(\gamma S_x x + \frac{\alpha_1}{2}\right) \cos^2\left(\gamma S_y y + \frac{\alpha_2}{2}\right). \tag{1.14}$$

It is particularly interesting when SP1 and SP2 are oriented along the same direction (together with their respective polarizers), for instance $\hat{x}$, each generating two beams with a separation S_x but with independent phase differences α_1 and α_2. In this case, the field after P3 reads

$$\begin{aligned}
E_{out_3} =& \frac{1}{2}\frac{z_R E_0}{z} \exp\left[-\left(\frac{z_R}{w_0 z}\right)^2 r^2 - i\tan^{-1}\frac{z}{z_R}\right] \exp\left[i\gamma\left(\frac{S_x^2}{4}\right)\right] \times \\
& \left\{\exp\left[i\gamma\left(x - \frac{S_x}{2}\right)^2 - i\frac{\alpha_2}{2}\right] \cos\left(\gamma S_x(x - \frac{S_x}{2}) + \frac{\alpha_1}{2}\right) + \right. \\
& \left. \exp\left[i\gamma\left(x + \frac{S_x}{2}\right)^2 + i\frac{\alpha_2}{2}\right] \cos\left(\gamma S_x(x + \frac{S_x}{2}) + \frac{\alpha_1}{2}\right)\right\}
\end{aligned} \tag{1.15}$$

$$\begin{aligned}
E_{out_3} =& \frac{E_G}{2} \exp\left[i\gamma\left(\frac{S_x^2}{2}\right)\right] \times \\
& \left\{\exp\left[-i\gamma S_x x - i\frac{\alpha_2}{2}\right] \cos\left(\gamma S_x(x - \frac{S_x}{2}) + \frac{\alpha_1}{2}\right) + \right. \\
& \left. \exp\left[i\gamma S_x x + i\frac{\alpha_2}{2}\right] \cos\left(\gamma S_x(x + \frac{S_x}{2}) + \frac{\alpha_1}{2}\right)\right\}.
\end{aligned} \tag{1.16}$$

If the conditions

$$\alpha_2 = \alpha_1 + 2\mu\pi \tag{1.17}$$

and

$$\gamma = \frac{\nu\pi}{S_x^2} \tag{1.18}$$

are fulfilled, for μ and ν integer numbers, eq. 1.16 is simplified to

$$E_{out_3} = \frac{E_G}{2}(-1)^\mu \left\{ \exp\left[-i(\frac{\nu\pi x}{S_x} + \frac{\alpha_1}{2} - \frac{\nu\pi}{2})\right] \cos\left(\frac{\nu\pi x}{S_x} + \frac{\alpha_1}{2} - \frac{\nu\pi}{2}\right) + \right.$$
$$\left. \exp\left[i(\frac{\nu\pi x}{S_x} + \frac{\alpha_1}{2} + \frac{\nu\pi}{2})\right] \cos\left(\frac{\nu\pi x}{S_x} + \frac{\alpha_1}{2} + \frac{\nu\pi}{2}\right) \right\} \tag{1.19}$$

and the intensity pattern of the output beam is written as

$$I_{out_3} = I_G \cos^4\left(\frac{\nu\pi x}{S_x} + \frac{\alpha_1}{2} + \frac{\nu\pi}{2}\right). \tag{1.20}$$

We generate an intensity pattern of the form $\sim \cos^4$ for ν even, and a pattern of the form $\sim \sin^4$ for ν odd. According to the condition given in eq. 1.18, these specific patterns can only exist at discrete propagation distances z_ν:

$$z_\nu = \frac{S_x^2}{\nu\lambda} \tag{1.21}$$

The farthest possible pattern from the source is the one with $\nu = 1$, since the point corresponding to $\nu = 0$ lies at infinity. However, $\gamma S_x^2/\pi$ in eq. 1.18 falls rapidly to zero, over distance. With a propagation distance of only a few times z_1, we can already find a very good approximation to the $\cos^4$ pattern which will continue propagating to infinity.

An interesting property of this technique is that we are able to repeat the splitting process, by adding more SPs and polarizers oriented in the same way, in order to obtain intensity patterns of the form cos^{2n}, with n being the number of SPs.

1.5 Propagation and scanning

The intensity patterns of the form $cos^2(k_x x)$ and $cos^2(k_x x)cos^2(k_y y)$, discussed in the previous section, are examples of structurally stable beams, since their

transverse intensity distribution remains invariant, up to scaling, under propagation [25, 26]. However, the pattern of light of the form $cos^4(k_x x)$ takes place at certain distances along the direction of propagation. This means that not every pattern originated with the described technique will be structurally stable.

Fig. 1.2 shows the effect that a combination of SPs has on an incoming beam for three different cases. The three resulting patterns (bottom row) are structurally stable. Dots represent the centers of the displaced outgoing beams. Arrows indicate the beam displacement that generates the corresponding SP. Crosses represent those points where two or more outgoing beams overlap their centers.

We have found that only when all dots are contained in a circle, the resulting pattern will have structural stability. For the cases that do not fulfill this condition, the patterns will change periodically along the direction of propagation. For the case shown in Fig. 1.2(c) this imposes a special phase and amplitude relationship during the splitting process, such that the beams with overlapping centers, outside of the circle, show total destructive interference. This does not apply to cases shown in Fig. 1.2(a) and (b) where, regardless of phase and amplitude relationships, the beam centers can be located inside a circle.

This result constitutes an interesting analogy with the condition that propagation invariant beams should fulfill. Only those patterns whose Fourier spectrum lies in the (k_x, k_y) domain in a ring, i.e., $k_x^2 + k_y^2 = a^2$, will propagate without changing their structure [27–31].

The structurally stable patterns of our technique are visible at every propagation distance, except for the small gaps (proportional to the lateral displacement) where the beams do not overlap. This property contrasts to the case of propagation invariant beams, like Bessel or Mathieu beams, where, for real experiments, the desired pattern is only found within a confined region.

As previously mentioned, it is possible to displace the generated beams in a continuous way by tilting the SPs, or stepwise by rotating the polarizers by 90°. The advantage of the latter method is that, contrary to the crystal tilting, it will be independent of the wavelength. By doing this we can, for instance, easily switch from a pattern $I = \cos^2(k_x x) \cos^2(k_y y)$ to $I = \sin^2(k_x x) \cos^2(k_y y)$, $I = \cos^2(k_x x) \sin^2(k_y y)$ or $I = \sin^2(k_x x) \sin^2(k_y y)$, depending on the polarizer that is rotated. Since the four modes are complementary, with these we can uniformly scan and illuminate the complete projection plane. Of particular interest is the case with three SPs, since, when properly aligned, they can produce the invariant hexagonal pattern shown in Figure 1.2 c). We can spatially displace this pattern by applying a π-phase delay to the three SPs (or alternatively a 90° rotation to
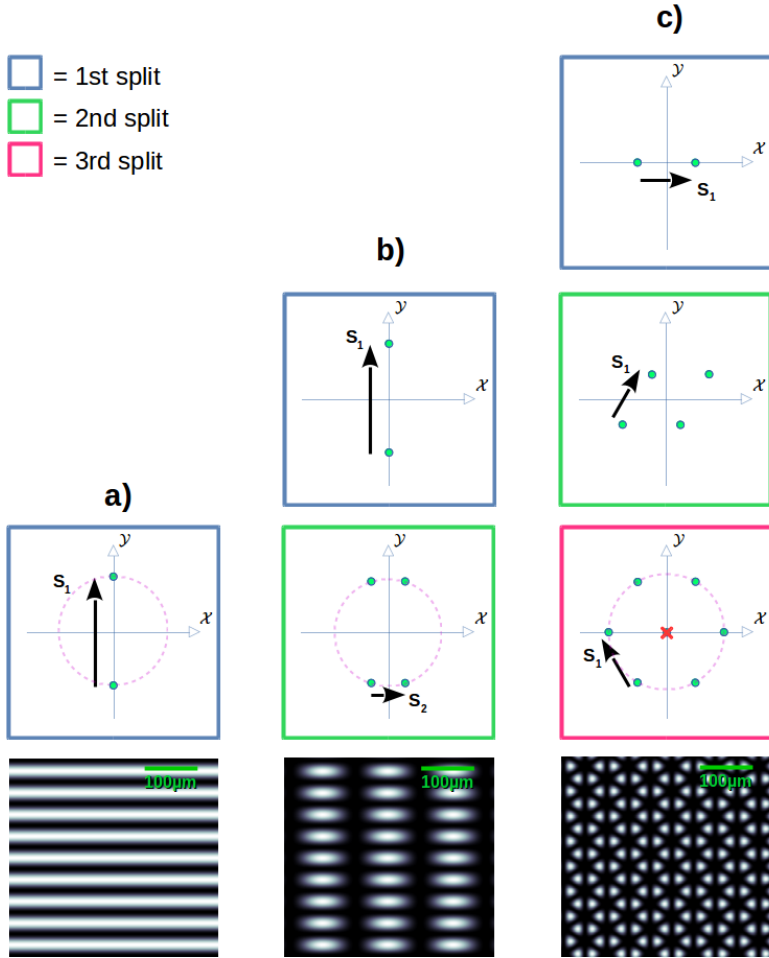
Figure 1.2: Diagrams of the series of splitting processes with one (a), two (b) and three (c) SPs, showing the resulting position of the beam centers as green dots after the splitting and displacement indicated by each arrow. From top to bottom the rows depict the centers of the resulting beams, step by step, for each splitting process. In c) the red cross over the green dot denotes the centers of two superposed beams with a phase such that they cancel out. The dashed circles show that for these cases (which propagate in a way that preserves the structure) all the beam centers lie within a circle. The bottom row shows the simulated modulation patterns for each case. The simulation was carried out with a Gaussian beam with a curvature radius of 5mm and a wavelength of 500nm. The displacement magnitudes are $S_1 = 60\mu m$ and $S_2 = S_1/3$).

the three polarizers before them), all at the same time, or if we do this to only the first, only the second or only the third SP (or polarizer). These combinations will respectively give the intensity patterns I_1, I_2, I_3 or I_4 in Figure 1.3. Since each of these patterns is invariant under propagation, a combination of exposures to these intensity patterns would result in a cumulative intensity pattern with a more complex structure, which would show the same propagation invariance. Some examples of the possible combinations are the cumulative intensities I_a, I_b and I_c depicted in Figure 1.3.

1.6   Experimental results

Setups similar to the ones in Figures 1.4 a) and b) were used to show some patterns that can be obtained. The light sources were LEDs with central wavelengths $\lambda_R = 617nm$ (FWHM=18nm); $\lambda_G = 530nm$ (FWHM=33nm) and $\lambda_B = 470nm$ (FWHM=25nm). The curved Gaussian beam was spatially filtered by a pinhole of $300\mu m$ diameter. The light patterns were recorded with an image detector at the projection plane.

In Figure 1.5 we can observe the different patterns that can be obtained from two independent SPs.

In the profiles in Figure 1.5 e) we can appreciate the modulation similar to $\sin^4$ (green line) which becomes evident due to a narrower peak and broader valley than for the $\sin^2$ modulation (blue line). It is important to note that the beam curvature $R = 45mm$ for this pattern is 11 times larger than the curvatures for the pure $\cos^4$ or $\sin^4$ states with $\nu = 1$, meaning that in Figure 1.5 c) we have only a good approximation of these states.

As can be observed in Figures 1.5 f) and g), with this technique we can easily obtain scalable patterns that preserve their structure. From Figures 1.5 h) and i) it is possible to see the potential of this technique for generating a variety of structures.
These results show the capability of the presented technique to shape even low-coherence light sources. Due to the small separation between the beams and the nature of the used elements, the patterns insensitive to external perturbations, such as vibrations or air turbulences.
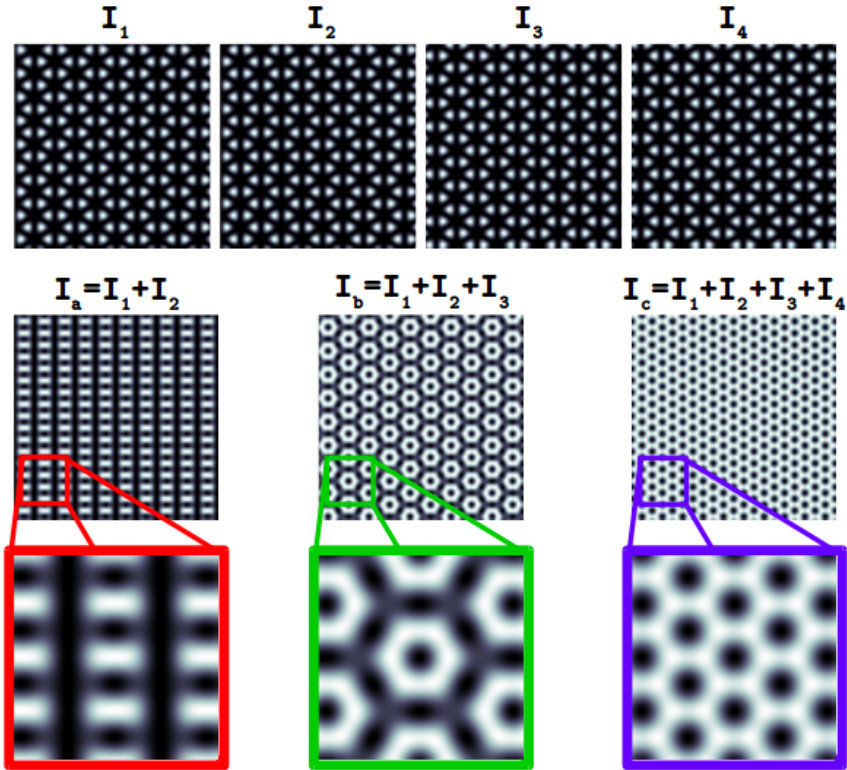
Figure 1.3: Top row: Simulated intensity patterns obtained with 3 SPs after inducing a π-phase delay (or rotating the polarizers by 90°) simultaneously to the three SPs (I_1), only to the first (I_2), only to the second (I_3) or only to the third SP (I_4). Center and bottom rows: Cumulative intensity patterns and close-ups from the resulting combinations: $I_a = I_1 + I_2$, $I_b = I_1 + I_2 + I_3$, $I_c = I_1 + I_2 + I_3 + I_4$
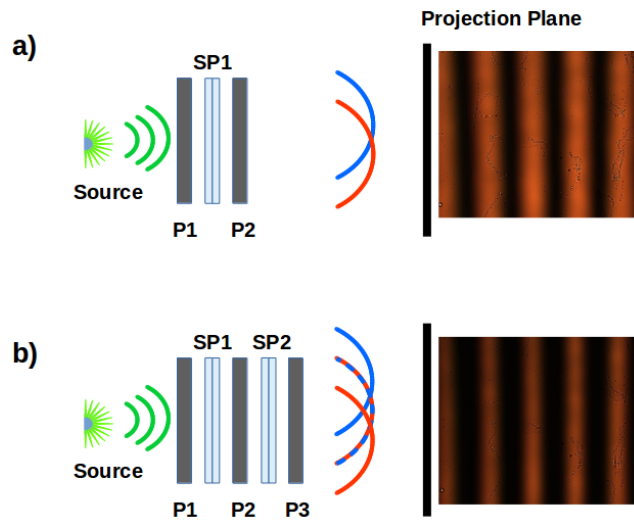
Figure 1.4: Experimental setups including a light source, linear polarizers P1,P2 and P3 and Savart plates SP1 and SP2, for generating $cos^2(k_x x)$ (a) and $cos^4(k_x x)$ (b) intensity patterns. Portions of the curved wavefronts of the split beams are depicted with an exaggerated separation for clarity.
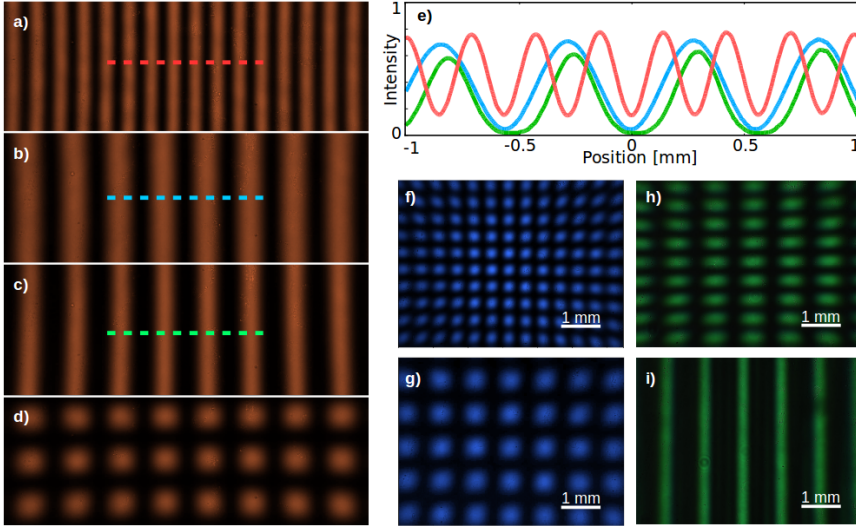
Figure 1.5: Normalized intensity modulations with a beam curvature $R = 45mm$, illumination at $\lambda_R = 617nm$ and displacements $S = 50\mu m$ for SP1 and SP2: a) $I = \sin^2(2\gamma Sx)$ for a configuration [P1][SP1][SP2][P2], with SP1 and SP2 aligned to double the displacement to $2S = 100\mu m$, b) $I = \sin^2(\gamma Sx)$ with [P1][SP1][P2], c) $I \approx \sin^4(\gamma Sx)$ with the configuration [P1][SP1][P2][SP2][P3], d) $I = \sin^2(\gamma Sx)\cos^2(\gamma Sy)$. e) Intensity profile along the dotted lines in a),b) and c) (red, blue and green lines respectively). Experimental patterns of the kind $I = \cos^2(\gamma Sx)\cos^2(\gamma Sy)$ for an illumination at $\lambda_B = 470nm$ with beam displacements $S = 50\mu m$ and beam curvatures $R = 45mm$ and $R = 95mm$ are shown in f) and g), respectively. Patterns at $\lambda_G = 530nm$ of the kind $I = \cos^2(\gamma Sx)\cos^2(2\gamma Sy)$ and $I = (\cos(\gamma Sx) + \cos(2\gamma Sx))^2$ achieved with two different beam displacements $S_1 = 50\mu m$ and $S_2 = 100\mu m$ in orthogonal and in parallel directions are shown in h) and i), respectively.

1.7   Applications

An important part of current imaging technologies for tissue tomography and 3D scanning relies on periodic light patterns with variable periodicity, position and wavelengths [14, 32, 33]. The technique that we present clearly meets all these requirements, making it a potential candidate for imaging techniques.

Another possible application is the shaping of the polarization states of a beam. The role of the polarizers in the setup can be seen as a filter for the polarization states of the displaced fields. If we discard, for example, the polarizer P2 in the setup shown in Figure 1.4 a), we will no longer detect changes in intensity . However the vectors of the polarization map will vary their direction in space according to $[cos(\gamma Sx), sin(\gamma Sx)]$. The polarization states can therefore be modulated in a similar way as for the intensity, in order to obtain complex polarization distributions.

Due to the versatility of the beams that can be generated with this technique, together with the robustness of the elements, we expect that it could play an important role for surface micro-structuring, specifically where large areas with periodic micro-patterns are needed such as photolithography, micro-lens fabrication and 3D printing. Since the optical elements involved in this approach can have high damage thresholds, this might be a good alternative to spatial light modulators and other commercial devices.
In addition, the system's ability to perform precise scanning means that more complex radiation patterns can be generated. In fact, the cumulative intensity pattern I_c in Figure 1.3 could be of particular interest for 3D printing since it allows to efficiently add a honeycomb micro-structure to larger volumes, increasing stability and reducing the amount of needed material.

In Figure 1.6, we show a proof of concept for photolithography and micro-lens production. UV light from an LED with a central wavelength $\lambda_{UV} = 385nm$ is used and a $\cos^2(k_x x)\cos^2(k_y y)$ modulation is applied to it (see Figure 1.6a). The light pattern is projected onto a glass slide covered with a uniform layer of a standard photo-sensitive polymer used for photolithography. The polymer that is exposed to the UV light undergoes a chemical reaction that allows it to be removed with a solvent. After development, the polymer surface resembles the illumination profile. For clarity, in Figure 1.6b) we show a 3D scan of the negative of these cavities. The actual z-profile, measured along the blue line, is plotted in Figure 1.6d).
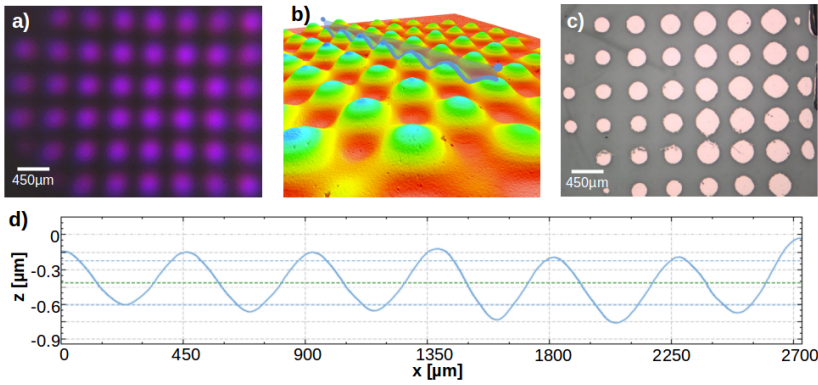
Figure 1.6: Proof of concept surface structuring using the proposed technique: a) Illumination pattern of the form $I = \cos^2(\gamma Sx)\cos^2(\gamma Sy)$ used for writing (central wavelength $\lambda_{UV} = 385nm$ (FWHM=10nm). b) Negative 3D profile of the developed photo-sensitive polymer after exposure to the illumination pattern (measured with SENSOFAR S neox Optical Profiler). c) Copper deposition on glass, revealing the over-exposed pattern on a photo-sensitive polymer. Variations in the intensity of the original beam lead to variations in the metallic spot sizes.

We could, for instance, use the resulting surface as a mold to cast a micro-lens array with a pitch of approximately $450\mu m$ where, by casting on a material of refractive index $n = 1.5$, the expected focal length of each micro-lens would be around 4cm. These parameters can be adjusted by placing the glass slide at a different distance, or by changing the pattern structure or the exposure time.

If we over-expose the polymer, the light pattern will produce regions where the glass is directly exposed. If we deposit material on the developed surface and dissolve the remaining polymer layer, the glass surface will be covered with the deposited material, revealing the shape of the intensity pattern. In Figure 1.6c), we see the results of applying this procedure and depositing copper on the over-exposed polymer. The copper circles are copies of the intensity pattern in Figure 1.6a). The different sizes in the pattern are due to differences in intensity in the illumination pattern and show how, by changing the dose of light, one may also change the final structure. In a similar way, UV light patterns can be used for 3D printing techniques (for example with UV-curable resin), by growing periodic structures in layers.

1.8   Conclusions

A technique for generating a variety of periodic intensity patterns with low-coherence and/or high energy light sources has been introduced. We have shown that it can be applied to micro-structuring of surfaces and it has some advantages, for specific applications, with respect to standard SLM devices.

The technique, as it is presented here, uses birefringent elements that split a curved beam and induce a lateral displacement. However, it is not limited to these kinds of elements and, specifically, not to Savart plates. For instance a Savart plate, as we use it here, could be replaced by a Nomarskii or Wollaston prism, followed by a lens to achieve the lateral displacement together with the desired beam curvature. The disadvantage of the latter configuration in comparison with the one that makes use of Savart plates is that it is not suitable for building a compact system and, depending on the configuration, it might not be suitable for low-coherence light.

Other compact birefringent materials that are out of the scope of this technique, but show potential properties for generating light patterns with different kinds of geometries, are the stress-engineered optical (SEO) elements [34, 35].

Chapter 2

Lens-free interferometric microscope: LIM

The information, text and figures in this chapter have been adapted, under the terms of the Creative Commons Attribution-NonCommercial license, from the original publication: "Ultrasensitive interferometric on-chip microscopy of transparent objects", Roland A. Terborg, Josselin Pello, Ilaria Mannelli, Juan P. Torres, and Valerio Pruneri. Science Advances, 2(6), 2016.

2.1 Abstract

Light microscopes can detect objects through several physical processes, such as scattering, absorption and reflection. In transparent objects, these mechanisms are often too weak, and interference effects are more suitable to observe the tiny refractive index variations that produce phase shifts. We propose a lens-free microscope design that makes use of two sheared and quasi-overlapped illuminating beams experiencing relative phase shifts when going through the object, and a complementary metal-oxide-semiconductor image sensor array to record the resulting interference pattern. Unlike conventional microscopes, the beams are unfocused, leading to a very large field of view (20mm^2) and detection volume (more than 0.5cm^3), at the expense of lateral resolution (35μm). The high axial sensitivity (<1nm) achieved using a novel phase-shifting interferometric operation makes the proposed device ideal for examining transparent substrates and reading microarrays of biomarkers. This is demonstrated by

detecting nanometer-thick surface modulations on glass as well as single and double protein layers.

2.2   Introduction

Since its invention, light microscopy has been evolving, and nowadays, a wide range of techniques are available to make visible what is invisible. Many microscopes rely on changes to the illumination beam that are introduced by the sample to be measured and associated with optical effects, including light scattering, absorption, reflection, or a combination of these. When none of these physical mechanisms can produce any detectable signal, which is often the case with highly transparent objects, such as biological cells and protein layers, one may still exploit phase shifts, that is, optical path differences (OPDs). This is the case, for example, with holographic [36–38] phase-contrast [39,40] or differential interference contrast (DIC) [41] microscopy. Alternatively one can interferometrically analyze the scattering signal from small particles and molecules [42, 43]. Most of these microscopes can offer high sensitivity, and resolution, up to single molecule detection. However, they also show a limited field of view (FOV) and depth of field (DOF) because light beams are focused onto the sample. One way to increase the FOV and DOF is to use low numerical aperture lenses or objectives, but this also reduces the resolution and sensitivity and increases the devices size. Recently, an intense research effort has been devoted to developing lens-free microscopes (LFMs), which work in a scattering or holographic configuration and can offer an unprecedentedly large DOF and FOV by using unfocused light beams and the full photosensitive area of a complementary metal-oxide semiconductor (CMOS) or a charge-coupled camera [3,11,12,44–49]. For example, Oh et al. [48] and Mudanyali et al. [11] described an LFM in DIC configuration that detects very small objects but does not demonstrate a large DOF nor a high axial sensitivity.

For many applications, like the microarray-based detection of biomarkers, a large FOV, large DOF, and high axial sensitivity become far more relevant than a high lateral resolution. In this chapter, we introduce a lens-free interferometric microscope (LIM) based on a novel design and physical phase-shifting interferometry (PSI) that make it possible to achieve a very high axial sensitivity and DOF.
We also show how the new scheme is able to measure nanometer-thick changes in the profile of a surface, mimicking, for example, defects or irregularities in

transparent materials, such as glass and polymers, and could also detect single and double protein layers. These initial demonstrations indicate the potential of the new platform, for example, in fast quality control of large-area glass substrates for displays or other consumer electronics products [50, 51], and the reading of microarray plates with a high number of biomarker targets [52–55].

2.3 Experimental setup and optical response

A scheme and a photograph of the actual LIM are depicted in Figure 2.1. The LIM uses simple components:a light emitting diode (LED) source, a CMOS image sensor array (ISA), two Savart plates (SPs) and two polarizers.
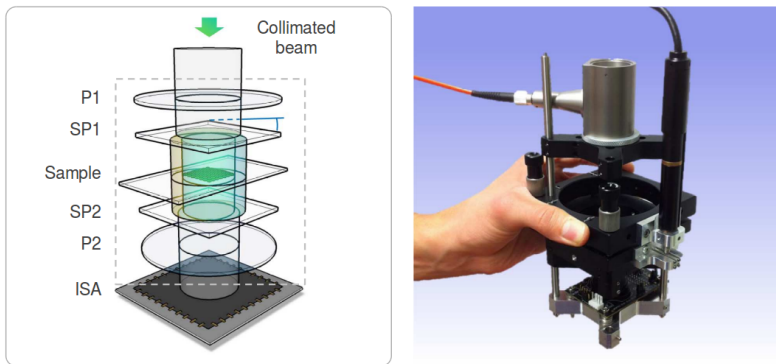
Figure 2.1: Scheme of the LIM, consisting of a light-emitting diode (LED) source followed by a fiber collimator (not shown in the scheme on the left) generating a collimated beam, a polarizer (P1), two SPs (SP1 and SP2), the sample in between the SPs, a second polarizer (P2) and a CMOS ISA. The photograph on the right shows an initial version of the device, built with commercial components.

To split the beam coming from the light source into two orthogonally polarized beams, conventional DIC microscopes use a Wollaston prism [41]. However, such a prism generates two orthogonally polarized beams that are not parallel, therefore requiring the use of lenses to alter the direction of propagation of the outgoing beams in order to make them interfere. Instead, the proposed LIM makes use of SPs that produce two nearly overlapping parallel and collimated beams.

The nature of the optical components in the LIM allows one to build a very

stable and compact setup (a minimal version of it fits perfectly into the palm of the hand). In Figure 2.2, we compare the schemes (not to scale) of the classical DIC and the LIM, showing the substantial difference in size, as well as the difference in the FOV in a measurement.
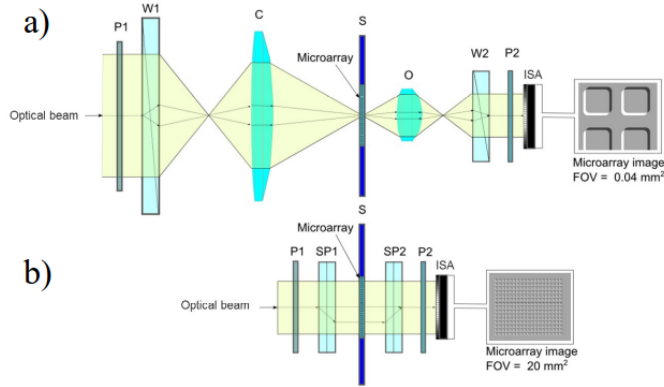
Figure 2.2: Comparison between a conventional differential interference contrast (DIC) microscope and the proposed LIM for detection of transparent microarrays. a) Side view of a conventional DIC microscope. Due to the fact that the light beams are focused, the lateral resolution is very high, but the field-of-view (FOV) is limited, allowing only part of the microarray to be seen. b) Side view of the proposed lens-free interferometric microscope (LIM). For the sake of clarity the scheme of the LIM has been enlarged, being in reality many times more compact than the DIC microscope. The use of unfocussed and collimated beams, allows a large FOV reading of the whole microarray. The axial sensitivity is similar to that of the DIC microscope while the depth-of-field (DOF) is three orders of magnitude larger (P: Polarizer, W: Wollaston prism, C: Condenser, S: Sample, O: Objective, ISA: Image Sensor Array, SP: Savart plate)

As described in chapter 1, each SP is composed of two birefringent crystals, which act differently on a light beam depending on its polarization. In Figure 2.3, we show in more detail the trajectory of the beams as they traverse the different elements in the LIM.

P1 is oriented at 45° in the transverse plane (xy) so that light entering SP1 contains an x-polarized beam (EPx) and a y-polarized beam (EPy) of equal amplitude. SP1 shears EPy with respect to EPx by a given distance S (in
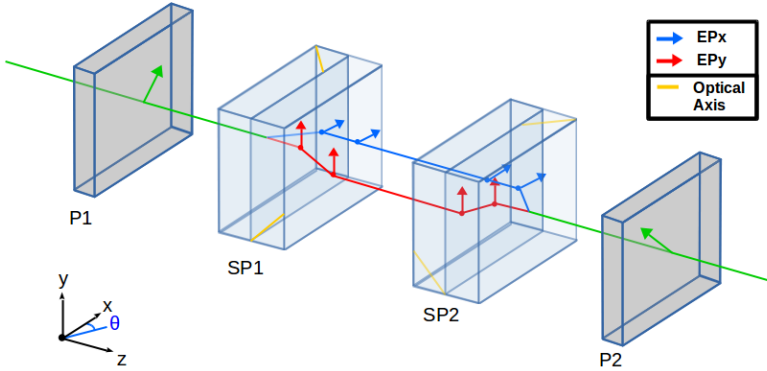
Figure 2.3: Trajectory of the beam centers in the LIM showing the input polarization, splitting, shearing, and projection to an orthogonal direction. Two SPs (SP1 and SP2) are placed between crossed polarizers (P1 and P2) to create a balanced Mach-Zehnder interferometer of partially overlapping and sheared beams with orthogonal polarizations.

this case, 25μm) in such a way that after exiting SP1, the two orthogonally polarized beams almost overlap and propagate in a parallel manner. After the beams traverse the sample region, SP2 exerts an equal and opposite shear $(-S)$ with respect to SP1 so that, in the absence of any sample, the two recombined beams perfectly superimpose as if there were no polarization-dependent shearing of the beams. Consequently, any phase non-uniformities occurring outside the detection volume between the SPs are intrinsically compensated for. On the contrary, any refractive index change introduced by the sample that affects EPx and EPy differently will lead to a detectable OPD by transforming the resulting phase difference into an intensity modulation using P2, which is orthogonal to P1.

In Figure 2.4, we show the typical interferometric response of the LIM with a transparent sample and a comparison to the case without the LIM. For the sake of clarity, we have omitted the diffraction effects, therefore these images represent the cases when the distance from sample to detector is negligible. Any object located in the beam path will lead to one of the following situations:

- If the object is located before SP1, the perturbation to the beam will be separated and reconstructed by SP1 and SP2. The resulting object image

will be equivalent to case 4 in Figure 2.4.

- If the object is located between SP1 and SP2, it will generate a double image. Each image corresponds to either the EPx or EPy beams going through the object (cases 2 or 3 in Figure 2.4).

- If the object is located after SP2, it will be illuminated by a beam that has already been separated and reconstructed. The resulting object image will be equivalent to case 4 in Figure 2.4.

In chapter 1, it was shown that, by tilting the SP, a relative phase delay α can be induced between the two sheared beams. From eq. 1.1 in chapter 1, we know that if SP1 suffers a very small tilt by an angle θ, Y being the rotation axis, then α will be directly proportional to θ.

By tilting only one SP, the LIM becomes unbalanced, and its working point changes. For example, the quadrature condition (that is, $\alpha = \pi/2 + m\pi$, with m being an integer) can be easily achieved. These points are characterized by a higher sensitivity to OPD changes, resulting in a lower threshold for detection. This also allows us to access the full range of the response of the LIM. In order to study the response of the LIM, for the sake of simplicity, we assumed uniform and monochromatic illumination at a given wavelength (λ), with the polarization set by the first polarizer aligned along the $(\hat{x}+\hat{y})/\sqrt{2}$ axis. When a transparent sample is present, any non-uniformity will produce an OPD between the two orthogonally polarized beams. The electric field at an arbitrary point in the detection plane can be described as

$$\vec{E} = \frac{E_0}{\sqrt{2}} e^{i\beta} [e^{i(\alpha_x+\phi_x)}\hat{x} + e^{i(\alpha_y+\phi_y)}\hat{y}], \tag{2.1}$$

where β is an arbitrary initial phase for both polarizations, α_x and α_y are the phase differences due to the tilt to the respective polarizations and ϕ_x and ϕ_y are the corresponding phase delays produced by the sample. After projection along the analyzer polarization (crossed polarization vector $\frac{\hat{x}-\hat{y}}{\sqrt{2}}$), the amplitude of the signal is

$$E = \frac{E_0}{2} e^{i\beta} [e^{i(\alpha_x+\phi_x)} - e^{i(\alpha_y+\phi_y)}]. \tag{2.2}$$

Assuming, without loss of generality, that the tilt in the SP only affects the horizontal polarization, i.e. $\alpha_x = \alpha$ and $\alpha_y = 0$, and that ϕ_x-ϕ_y=ϕ, from eq. 2.2 it follows
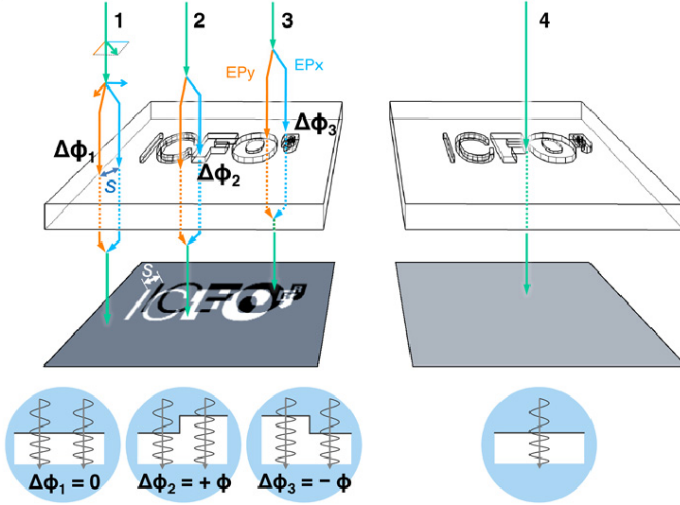
Figure 2.4: System response of a transparent sample, without considering diffraction, in the LIM device (left scheme) and in a non-interferometric setup (right). In the LIM, two orthogonally polarized beams (EPx and EPy) are symmetrically sheared by a distance S. Depending on the presence of spatially dependent relative phase shifts between them, an intensity pattern is detected on the ISA. By tilting SP1, an initial phase shift α between EPx and EPy can be introduced in order to maximize the sample detection. For instance, for $\alpha = \pi/2$, a relative phase-shift $\Delta\phi_1 = 0$ caused by the sample produces an intermediate intensity (gray zone), whereas $\Delta\phi_2 = +\phi$ and $\Delta\phi_3 = -\phi$ produce clearer (white) and darker (black) zones, respectively. In contrast, there is no formation of any image pattern when light (beam 4) propagates through the transparent sample in a non-interferometric configuration.

$$E = E_0 e^{i(\beta + \alpha/2 + \phi/2)} \sin(\frac{\alpha + \phi}{2}). \tag{2.3}$$

This corresponds to an intensity

$$I(\alpha, \phi) = I_0 \sin^2(\frac{\alpha + \phi}{2}), \tag{2.4}$$

where $I_0 \propto |E_0|^2$. Since $\sin^2(x) = \frac{1}{2}[1 - \cos(2x)]$, then

$$I(\alpha, \phi) = \frac{I_0}{2}(1 - \cos(\alpha + \phi)). \tag{2.5}$$

Experimentally, we have confirmed that, for the LIM configuration with visible and near infrared light, a bias phase α between EPx and EPy in the 2π to 2π range could be introduced as well, without producing significant changes in beam separation (shear) or image displacement. The latter ones could not be detected because they always remain much smaller than our xy resolution limit. Similarly, we have assessed that α is linear with respect to small SP tilt angles as can be confirmed in Figure 2.5, where the expected sinusoidal intensity variation can be properly fitted.

2.4   Image Acquisition and Analysis

In general, image sensors measure only light intensity. To retrieve information from the phase variations in a transparent sample, we use the LIM to translate them into intensity changes (interferograms), which can be detected by the ISA. However, these interferograms need to be processed prior to obtaining the information from the phase variations. In Figure 2.6, we show an overview of the steps required to retrieve an OPD map with high sensitivity, and how the image quality is enhanced after every step.

When the measurement process is started in the LIM, 20 to 50 interferograms are captured by the ISA, for different tilt positions of the SP1. For each tilt position, the illumination spectrum is scanned, alternatively, for only Red-Green-Blue (RGB) LEDs, all wavelengths can be used at the same time and separated later using the RGB filters of the ISA (in this case, a special algorithm that eliminates the cross-talk between color channels is used).

Each illumination wavelength is processed independently by a phase-shifting
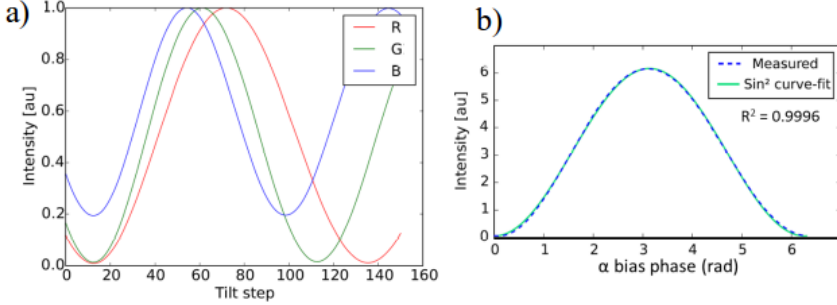
Figure 2.5: Measured optical transfer function of the LIM. a) Relation between the mean intensity captured by the ISA and the tilt step of SP1 (in this case, 120 steps = 1.01°) for 3 different illumination colors (λ = 465, 515 and 635nm for R, G and B, respectively). b) Sinusoidal fit of the transfer function for red light (λ = 635nm). The fact that the transfer function follows a nearly perfect sinusoidal shape (R^2 = 99.96%) confirms the linear relation between the SP tilt angle and the OPD between the two sheared beams.

algorithm (see below for more details). The output at this point is the complex field of the diffracted beam. With standard propagation algorithms, we can calculate the refocused image at the sample plane and apply further image reconstruction algorithms (detailed below). For samples where the changes in the optical properties are negligible over the illumination spectrum, the noise and unwanted diffraction artifacts can be significantly decreased by averaging the responses of all the colors.

By taking comparative measurements with and without a sample, we are able to further reduce noise, whose origins are illumination inhomogeneities and other imperfections in the optical elements.

High axial sensitivity images have been achieved with as few as 20 tilt positions of the SP1, covering the whole transfer function of the LIM. Using video mode, the acquisition time can be faster than 5s. The processing time needed to extract the OPD from the raw images is typically around 30s per wavelength-set, on a regular central processing unit (Intel Core i5). Most of the processing time is devoted to determining the relation between the tilt position and the phase-shift α. For applications that need a faster response, this procedure can
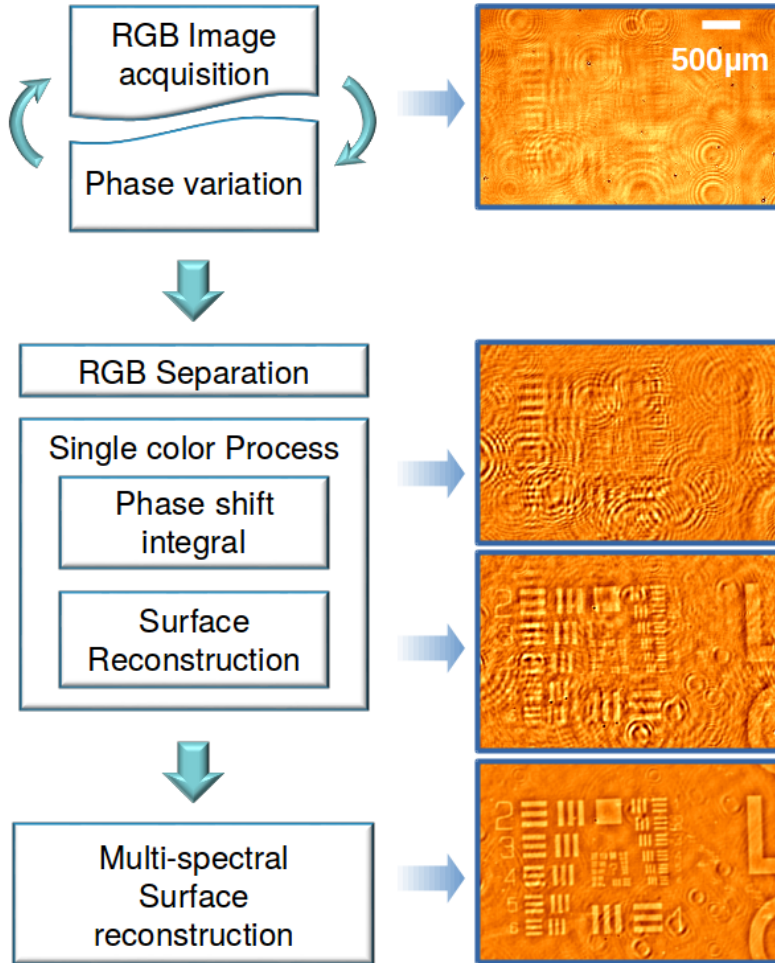
Figure 2.6: Left: Workflow used in the acquisition and analysis of our measurements. Right: Raw intensity capture (top) and OPD outputs at each step of the process. The measured sample is a transparent glass slide with silica patterns of only 10nm thickness.

be significantly sped up by using previous knowledge of the tilting position and parallelized computing. In Figure 2.7, we compare the LIM with a commercial DIC microscope by measuring, with both systems, a glass sample with transparent silica patterns of 10nm thickness. The XY resolution of the LIM is $\sim 35\mu$m for this configuration when the sample is at a distance of 30mm from the ISA. This value can be improved by reducing the distance between the sample and the ISA. The FOV in this DIC microscope is 4 times smaller than the one in the LIM.
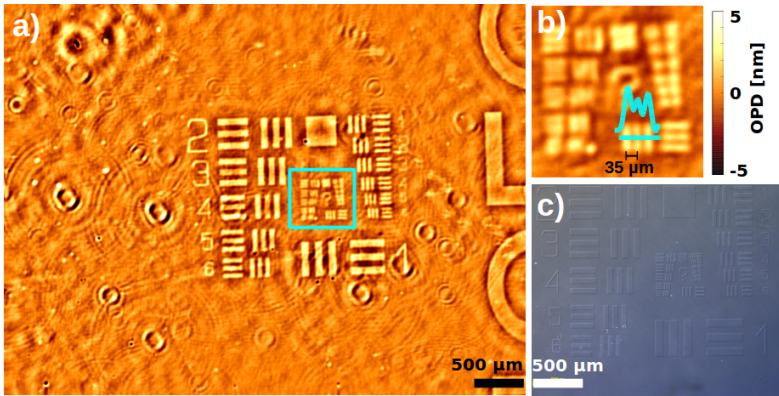
Figure 2.7: Side by side comparison between the LIM and a commercial DIC. a) Full OPD map of a 10nm-thick silica USAF-resolution test target on glass captured with the LIM (wavelengths: $\lambda = 465$, 515 and 635nm). b) Zoom-in to the blue box in a), showing that the XY resolution of the LIM is $\sim 35\mu$m. c) Same sample imaged using a commercial DIC microscope at the lowest magnification. .

2.4.1 Phase-Shifting interferometry (PSI)

Phase-shifting digital holography (PSDH) is a well-established technique [56] for retrieving phase information from intensity images. It requires the detection of four interferograms, which are generated by interfering the sample beam (containing the phase information to be retrieved) with a reference beam that can have one of four specific phase delays ($\alpha = 0$, $\pi/2$, π, $3\pi/2$) with respect to the sample beam. For a given sample's phase variation (ϕ), one obtains a set of intensities ($I(\alpha, \phi)$).

According to PSDH theory, as described by Malacara [57], ϕ can be calculated as

$$\phi = \tan^{-1}\left[\frac{I(\pi/2,\phi) - I(3\pi/2,\phi)}{I(\pi,\phi) - I(0,\phi)}\right]. \tag{2.6}$$

However, when α cannot be precisely set or is not uniquely defined (as is the case in multi-spectral imaging), it is more practical to obtain a larger set of interferograms in the range $0 \le \alpha \le 2\pi$ and analyze them using a novel PSI method, which works in the following way.

Firstly, we define the weight functions

$$\Gamma_{\sin}(\alpha) = \frac{\sin(\alpha)}{\pi[n+m]}, \tag{2.7}$$

and

$$\Gamma_{\cos}(\alpha) = \frac{\cos(\alpha)}{\pi[n+m]}. \tag{2.8}$$

In the LIM, the intensity in an interferogram is given by eq. 2.5. When integrating the different interferogram intensities with each weight function over a complete period of α, we obtain the PSI values

$$\Psi_{\sin} = \int_{-2m\pi}^{2n\pi} I(\alpha,\phi)\Gamma_{\sin}(\alpha)\mathrm{d}\alpha = \frac{I_0}{2}\sin(\phi) \tag{2.9}$$

and

$$\Psi_{\cos} = \int_{-2m\pi}^{2n\pi} I(\alpha,\phi)\Gamma_{\cos}(\alpha)\mathrm{d}\alpha = -\frac{I_0}{2}\cos(\phi) \tag{2.10}$$

From these PSI values, we can calculate, in an independent form, phase and intensity

$$\phi = -\tan^{-1}\left[\frac{\Psi_{\sin}}{\Psi_{\cos}}\right], \tag{2.11}$$

and

$$I_0 = 2\sqrt{{\Psi_{\sin}}^2 + {\Psi_{\cos}}^2}. \tag{2.12}$$

To verify the results from the proposed PSI method, we have carried out simulations under similar conditions to the ones in our LIM. In Figure 2.8, we can observe the effectiveness of this method to retrieve even the smallest phase signal from a set of interferograms, where effects from absorption and OPD from a non-transparent sample are mixed.
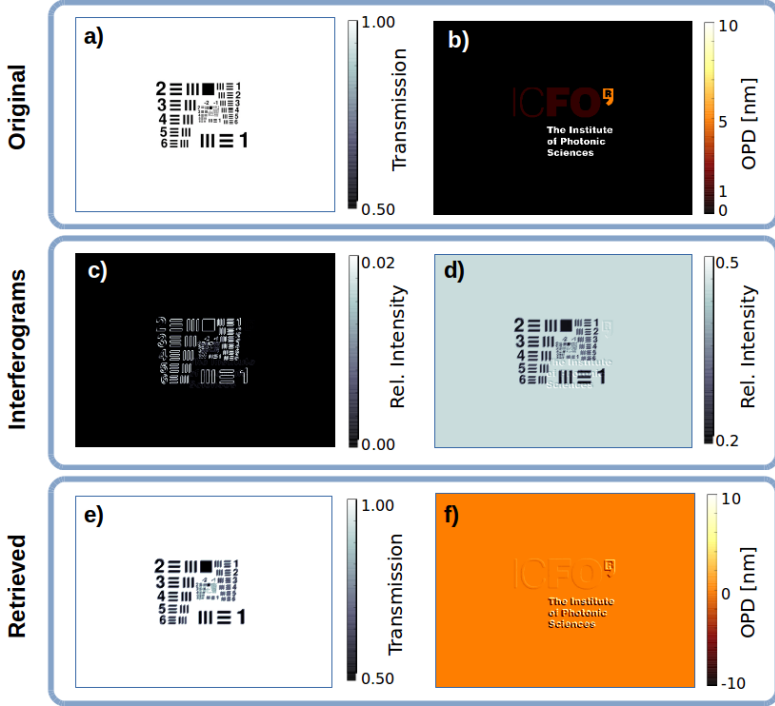
Figure 2.8: PSI simulations were carried out using the same parameters of the LIM when illuminated with light at $\lambda = 635nm$ and with diagonal shear of 50μm. The distance from sample to detector is 0 for clarity. Top row: transmission (a) and phase (b) variations introduced by the sample. The minimum transmission for the sample is 50%. The OPD (phase) in the logo takes the values 1, 5, and 10nm. Center: Simulated interferograms for the cases $\alpha = 0$ (c) and $\alpha = \pi/2$ (d). It is possible to see the characteristic double-image footprint of the system and a mixed signal of the transmission and phase maps. Bottom: Recovered transmission (e) and phase (f) maps after applying our PSI method with 40 interferograms. The retrieved transmission and phase show the expected differential effect from the SP (OPD values of $\pm 1, \pm 5$ and ± 10nm). It should be stressed that the method is very robust and errors are minimal, since the two maps have been successfully decoupled, even though transmission effects here are much stronger than the phase effects (which are smaller than $\lambda/600$).

2.4.2   Image Reconstruction

The transmission and OPD maps obtained with the PSI method can be used to calculate the complex optical field $E(z_0)$ at the detector plane. Because of the nature of the SPs, the information obtained with the PSI method is encoded as a duplicated (and shifted) image of the sample, as shown in Figure 2.4. Furthermore, because the distance between the sample and the ISA (up to 30mm in our experiments) is much larger than λ, the recorded pattern is diffracted with respect to the sample pattern. To retrieve the original optical path distribution, numerical image processing is required.

The first step is to use a standard Fresnel propagation algorithm [58] to calculate the field at the sample plane, i.e., $E(z_{sample})$. The phase of this field contains the refocused OPD map of the sample. The correct sample plane distance can be easily found from prior knowledge of the distance from sample to ISA. If needed this process can also be automatized, by using one of several auto-focusing algorithms in the literature [59].
To compensate for the double-image effect in the map, which means to obtain the source image, one could use a deconvolution algorithm, taking into account the LIM's point-spread function (roughly consisting of two Dirac delta functions). However, this method does not give good results as it enhances the noise in most cases.

A simple solution is to calculate $E(z_{sample})$ and $E^*(z_{sample})$ (where E^* is the complex conjugate of E), which give the OPD maps depicted in Figures 2.9 a) and b), respectively. Both images look very similar except for the 'shadows' of the patterns, which are cast in opposite directions. This suggests that in one case, we are mainly refocusing the information carried by EPx (while defocusing EPy), whereas in the other case, we are refocusing EPy (while defocusing EPx). After compensating for the relative displacement S between the images, we can average them to obtain a smooth image in c). This method can be complemented with iterative methods, to further decrease the noise [60].

2.5   Results

To demonstrate the potential for applications of the LIM, we designed three different experiments with transparent samples of differing natures.
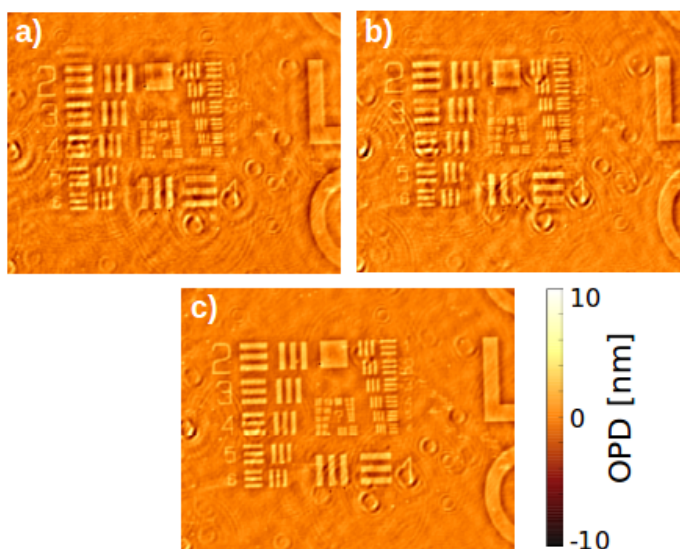
Figure 2.9: OPD maps of a transparent sample, obtained by propagating to the sample plane, from the complex field calculated by the PSI algorithm (a) and the complex conjugate of the same field (b). It is possible to see a difference in the direction of the 'shadows', especially for the larger objects, indicating that in one case we are focusing EPx and in the other case, EPy. c) Average of the maps in a) and b) after compensating for the relative displacement S due to the shear of the SP. The 'shadow' effect and general background noise have significantly decreased.

The first was aimed at measuring OPDs embedded in the material, i.e., without changes in the topography of the sample. Therefore, we designed a sample with a transparent indium tin oxide (ITO) ribbon which increased its temperature when we applied an electric current. A temperature gradient across the sample was generated and, through the thermo-optic effect, a spatial gradient of refractive index was also generated.

The second sample was designed for benchmarking the detection of microarrays. A matrix of small dots of silica with different thicknesses was deposited on a glass substrate.

The third sample was designed to show the potential for biomarker detection. A microarray of bovine serum albumin (BSA) monolayers was prepared on a glass substrate. The increase in OPD of the array was measured after it was covered with a monolayer of antibodies with affinity to BSA.

2.5.1   Thermo-optic refractive index gradient detection

A transparent ITO ribbon (10nm thick, 0.5mm wide and 7mm long) was deposited on a glass substrate, as shown in Figures 2.10 a) and b). Because of the Joule and thermo-optic effects, the temperature and local refractive index of the ribbon and the glass beneath increased. An independent thermography (Figure 2.10 c)) revealed a maximum temperature of about 60^oC, with a lateral gradient across $S = 25\mu$m of only 1^oC. Consequently, an increase in the image intensity was detected in the LIM when increasing the injection current, as shown in Figure 2.10 d). Since the temperature gradient was not stable enough over the time needed for the acquisition, a full PSI analysis could not be carried out.

For a refractive index change along the direction of the shear, the OPD can be estimated to be equal to $[n(x) - n(x\text{-}S)]\times d$, with d being the thickness of the glass substrate, and n(x), the refractive index at position x, obtained from the thermo-optic coefficient dn/dT and the local temperature increase ΔT(x) (where ΔT(x)-ΔT$(x - S)$=1^oC).

Using n(x) = n(0^oC) + dn/dT$\times\Delta$T(x) and a value of the thermo-optic coefficient $\sim 10^{-5}K^{-1}$ [61], we obtained a difference of about 10^{-5} refractive index units for two points separated by the shear distance. If we multiply this number by the thickness of the substrate (1mm), we can estimate the corresponding maximum detected OPD to be about 10nm. For this, we assumed the lateral

temperature gradient to be constant throughout the whole thickness. Thus, the real OPD values are likely to have been even smaller.

This measurement makes it evident that the LIM can be used to detect certain kinds of inhomogeneities and defects in transparent materials.
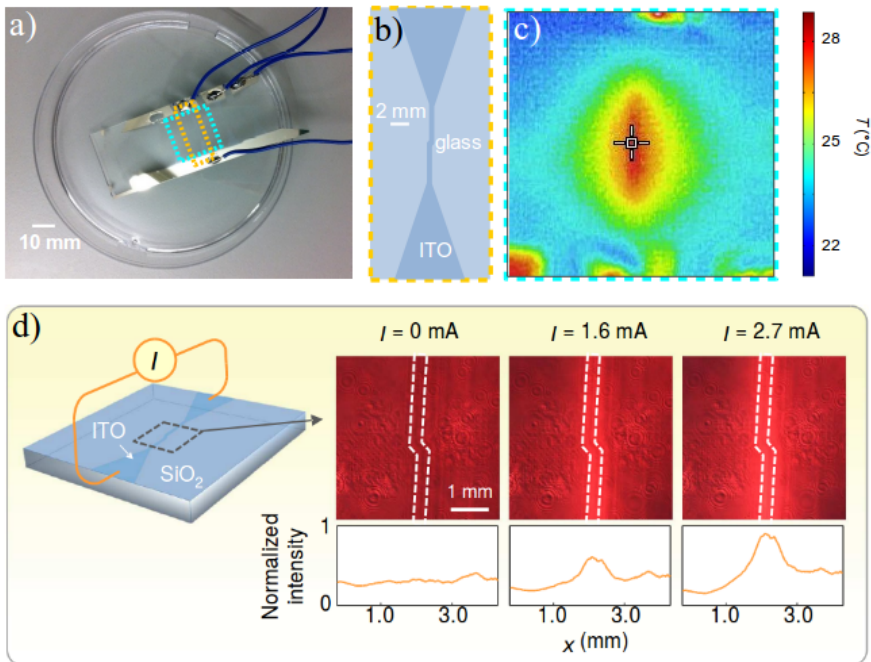
Figure 2.10: a) Real picture of the ITO ribbon deposited on a glass substrate and connected to soldered electrical wires. b) Schematic of the 7mm x 0.5mm ITO ribbon and triangular pads used for connection. c) Thermography obtained with an infrared camera, showing the temperature distribution for a current of 1mA. d) Images of refractive index (phase-shift) patterns induced through the thermo-optic effect, when injecting electric currents (I) of 0, 1.6, and 2.7mA, respectively. The largest OPD is estimated to be 10nm.

2.5.2 Microarray detection

The second set of samples consisted of ultra-thin silica dot patterns on a silica substrate, as depicted in Figure 2.11 a). Thicknesses of d = 2 and 5nm were deposited by electron beam evaporation and measured for comparison by atomic force microscopy (AFM). The corresponding OPDs recovered from the LIM agreed with the AFM measurements. For example, the measured OPD of the thinnest sample was about 1nm, which, considering the refractive index of silica (n = 1.45) [61], corresponds to a physical thickness [OPD/(n-1)] of the silica pattern of about 2.2nm, in agreement with the AFM measurement (about 2nm). A small area evidencing the details of the silica pattern is shown in Figure 2.11 a). However, the images in our work always covered the full 20mm^2 FOV of the ISA.

The third sample consisted of protein layers deposited on a glass substrate. An array of monolayer spots of BSA was deposited on epoxysilane-coated glass [62] using a sciFLEX-ARRAYER S3 spotter from Scienion, as depicted in Figure 2.11 b). After incubation with anti-BSA immunoglobulin G (IgG), which specifically binds to BSA, and rinsing, the BSA monolayer spots were converted to BSA + IgG bilayer spots. Measurements of both monolayer and bilayer arrays in the LIM gave a clear signal. The retrieved OPDs were 0.7 and 1.8nm, respectively. For simplicity, we can assume that, after drying, each protein layer collapses in a dense layer of thickness proportional to the molecular weight of the protein. Because the molecular weights of BSA and IgG are 66 and 150kD, respectively, if each BSA molecule had captured an IgG molecule, then the expected ratio in the OPD would have been 3.3 [∼(150kD + 66kD)/66kD], which is slightly higher than the observed value of 2.6 (∼1.8nm/0.7nm). This suggests that most of the BSA proteins captured an IgG protein.

2.6 Conclusions

The proposed LIM design has several unique features. First, the opposite shears introduced respectively by SP1 and SP2 have the same effect on the optical path of the two beams EPx and EPy, thus ensuring a perfectly balanced interferometric configuration when no sample is present. This means that the LIM can work with a light source having a relatively short coherence length, with the advantage of strongly reducing detrimental effects such as standing wave patterns due to spurious reflections and speckle [58]. The coherence length of the light
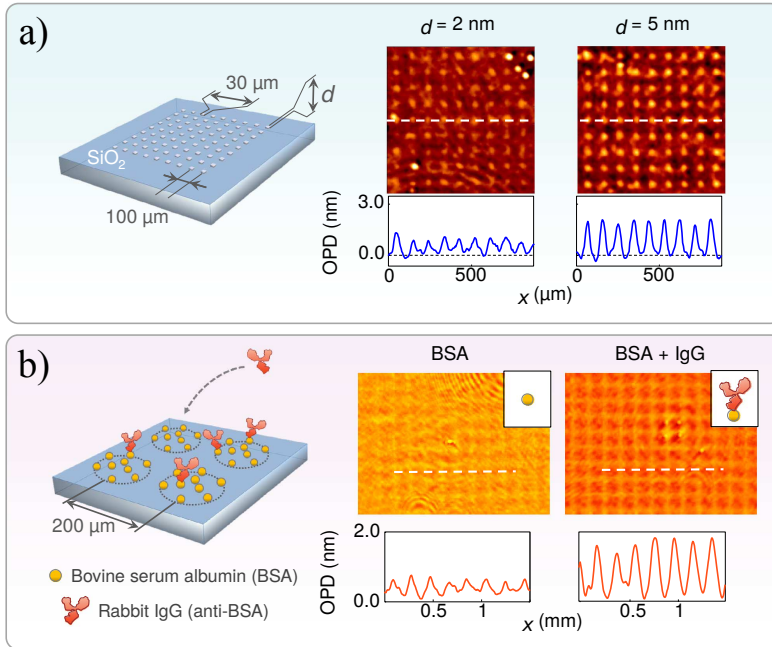
Figure 2.11: a) Silica dot patterns of different thicknesses (d) on a silica substrate are detected (spot diameter = 30μm, pitch size = 100μm). The measured OPD profiles (bottom graphs) agree with the thicknesses measured, using AFM, of 2 and 5nm, respectively. b) Detection of monolayer and bilayer protein arrays (spot diameter = 100μm, array pitch = 200μm). BSA monolayer spots after deposition on epoxysilane-coated glass and after incubation with anti-BSA IgG and rinsing. Both interferometric images and cross sections with OPD values are shown.

source only needs to be larger than the OPDs to be detected. If we are interested in OPDs of less than 100nm, incoherent light sources like LEDs become very suitable. In our experiments, the source was a multicolor LED system emitting at 465, 515, and 635nm with a coherence length of 6μm.

Second, each point of the EPx beam interferes with the corresponding sheared point of the EPy beam. This is an ideal situation for detecting periodic patterns with dimensions equal to or larger than the shear distance S which makes the proposed LIM particularly effective in reading biomarker microarrays. This was demonstrated above by detecting multiple spots of single and double protein layers. The shear distance S can be as small as the distance between two adjacent pixels, meaning that with the demonstrated configuration, thousands of biomarkers could be detected simultaneously by exploiting the full FOV. Third, the small distance S between interfering points confers high stability to the device because potential mechanical and thermal fluctuations have similar effects on closely spaced regions and, thus, do not influence the relative OPD.

Fourth, contrary to microscopes that focus light, the FOV, DOF, and axial sensitivity are independent parameters, and the LIM has a DOF limited only by the physical space between the two SPs. This means that it can detect OPDs not only on the surface, as we did in the experiments, but also inside the volume of an object. In our experiments, this was demonstrated by placing the samples at various axial positions, up to 30mm away from the ISA, and confirming that the quality of the detection (images) did not degrade appreciably. The experimental DOF of 30mm was associated with a lateral resolution of 35μm. Note that, if necessary, the lateral resolution can be significantly improved at the expense of DOF and detection volume. Finally, the optomechanical alignment and assembly of the device are straightforward because the optical beam is of large dimensions and is not focused.

In conclusion, we have introduced and demonstrated a new interferometric microscope that combines DIC microscopy and LFM, with a novel PSI operation. Similarly to the DIC, it allows detection of transparent samples with nanometric axial sensitivity and, at the same time, it provides large FOV and DOF, as do other LFMs. Besides optical performance, its simplicity and high optomechanical stability confer significant impact potential for a wide range of applications, such as quality inspection of spatial patterns and defects in glass and polymer materials, in-line control of their fabrication processes, and label-free reading of large microarrays of multiple biomarkers. The new device is low-cost and compact, is suitable for point-of-care applications and may even become an accessory or be fully integrated in handheld devices in the future.

Chapter 3

The LIM as a portable reader for plasmonic biosensors

The information, text and figures in this chapter have been adapted, under the terms of the Creative Commons CC BY license, from the original publication: "Phase-sensitive plasmonic biosensor using a portable and large field-of-view interferometric microarray imager", Filiz Yesilkoy, Roland A Terborg, Josselin Pello, Alexander A Belushkin, Yasaman Jahani, Valerio Pruneri & Hatice Altug. Light: Science & Applications volume 7, page 17152 (2018)

Author contributions: FY, RT, JP, VP and HA designed the experiments and conceived this study. VP proposed the EU Horizon 2020 RAIS project. FY performed the numerical computations. FY and YJ designed and fabricated the plasmonic chips. FY and AB performed the bio-experiments. FY, RT, JP and AB developed the code for data processing and prepared the data. FY, VP and HA wrote the paper with contributions from all authors.

3.1 Abstract

Plasmonics can enhance light-matter interactions, making it an effective platform for sensing applications. For biosensing, plasmonic devices have been

mainly designed to exploit their intensity and spectral changes. Phase variations of plasmonic devices have not been studied to the same extent, although they potentially show greater sensitivity, mainly due to the complicated optical systems needed for this purpose. In this chapter, we present a system based on the combination of specifically designed plasmonic gold nanohole arrays, together with our lens-free interferometric microscope (LIM). We show that such plasmonically enhanced LIM allows the detection of atomically thin (angstrom-level) topographical features over large areas, enabling simultaneous readings of thousands of microarray elements. It also makes use of scalable techniques, as well as low-cost commercial electronic and optical elements, making it a good candidate for point-of-care biomarker detection applications.

3.2   Introduction

Biosensing without special personnel or infrastructure is essential for the biomedical community in order to be able to deliver on-site diagnostics [7, 8, 63]. Other fields, such as food safety and environmental surveillance, could also profit from robust and affordable technologies that detect multiple analytes within a short time and with small sample volumes [64].

Nanophotonic techniques are used to enhance light-matter interactions by means of sub-wavelength confinement and amplification of optical near-fields. Therefore, they become an attractive solution for problems in biosensing applications where very small quantities of material need to be detected in real-time, with high sensitivity and in a label-free way [65–74]. In addition, plasmonically enhanced fields act over very short distances; this is exploited as a way to enhance only the signal from extremely small volumes that are very close to the sensing surface, while decreasing other possible sources of noise.

In particular, sensors based on surface plasmon resonance (SPR) [75] and localized SPR (LSPR) [76, 77] have demonstrated new possibilities for optical label-free detection, as an alternative to cumbersome and time-consuming techniques like enzyme-linked immunosorbent assay (ELISA) or fluorescence detection.

Clinically relevant detection limits of various biomaterials (such as bacteria, viruses, exosomes and proteins) have been achieved by performing far-field spectral intensity measurements with plasmonic devices [78–81].

Because of their simplicity, optical plasmonic sensors have been proposed as point of care (POC) devices [82–85]. These sensors measure far-field intensity changes due to shifts in the sharp plasmonic resonances when illuminated with narrow-band light sources, using ,in some cases, commercial devices like

cellphone cameras. These techniques avoid the use of bulky and cumbersome equipment, but the sensitivity of the system is usually limited by the plasmonic resonance mode, as well as the ambient and instrument noise.

For most plasmonic devices, especially the ones using microscopes, high-throughput and multiplexed detection schemes are not possible. Therefore, the main challenges for nanoplasmonic sensors are the need for simple and robust optical readout systems as well as low-cost and scalable production.

In order to enhance the sensitivity of SPR sensors, Kabashin et al. [86] introduced a different detection scheme. Instead of the typical detection of spectral intensity shifts, they have exploited the sharply varying phase shifts close to resonance, first reported by Abeles et al. [87]. Plasmonic detection schemes based on phase have shown that the refractive index sensitivity of SPR sensors could be improved [88, 89].

Despite the success of phase detection for SPR techniques, examples where the same detection scheme is applied to LSPR sensors are rather limited [90–92]. Typical phase-sensing techniques are not well suited for POC applications, since they tend to need bulky instruments or to use detection schemes that are very sensitive to ambient noise. Moreover, multiplexed high-throughput detection schemes are not usually simple to implement on these kinds of techniques.

In chapter 2, we introduced the LIM as a system that offers ultrasensitive axial topographic resolution in a lens-free and compact form, together with a large field of view (FOV). By detecting spatial phase variations in a collimated beam, it was possible to detect arrays of protein monolayers. However, the sensitivity was not sufficient for biosensing applications, where smaller concentrations and smaller biomarkers need to be detected.

In this chapter, we present a new plasmonic phase-sensitive detection platform for measuring biomarker microarrays with high throughput, combining the LIM and specifically designed LSPR chips, formed by gold nanohole arrays (Au-NHAs). The nanostructures enhance the phase effects of near-field light-matter interactions, which are later detected at the far-field using the LIM.

For the first time, we exploit the sharp phase transitions at the resonances of plasmonic Au-NHAs [93], instead of using the standard amplitude-based approach. We improve the sensitivity of the LIM by more than one order of magnitude and, at the same time, we demonstrate high-throughput plasmonic biosensing using the LIM, which is crucial for efficient biomarker detection.

3.3 Experimental Setup

Figure 3.1a) depicts the scheme for the reading of large-area plasmonic chips with the LIM configuration. In order to build an integrated version of the LIM, the polarizers have been glued to their respective SPs with an optical adhesive (NOA63 from Norland Products Inc). These are depicted in the scheme as a single element, where the SP is always facing towards the sample. The alignment and the optical response of the LIM are the same as in chapter 2.

The plasmonic chip is placed in the sensing volume with the gold surface facing towards the light source. This optical design allows for the projection of minute topographical changes, enhanced by the plasmonic interaction, onto the image sensor array (ISA). The ISA in this case is a complementary metal-oxide semiconductor (CMOS) sensor, similar to the one in chapter 2.

These elements are integrated into a full reader, shown in Figure 3.1g), designed for use with microfluidic cartridges. The total dimensions of the integrated system are 23cm × 21cm × 15cm and contain the light source, optical elements and electronics. The light source is a light-emitting diode (LED) block, with LEDs at wavelengths that are chosen to spectrally overlap with the transmission peak positions of the plasmonic chip: two in the red wavelength region (625 and 656nm) for 'dry' and two in the near-infrared (850 and 870nm) for 'wet' medium measurements. The electronics in the system control a stepper motor, which is used to generate precise tilts of the SP, with angles of up to $\pm\, 2^o$.

The plasmonic chip consists of uniformly nanostructured Au-NHA, each hole with a 200nm diameter and 600nm period, covering its entire surface. This is fabricated on robust glass wafers, as shown in Figure 3.1b), and then covered with 10nm of titanium (adhesion layer) and 120nm of gold. The Au-NHAs are fabricated using deep-ultraviolet lithography and ion beam etching. A statistical analysis of the performance of the chips produced with these large-scale fabrication techniques has shown that they are exceptionally robust and their optical parameters are consistent. We found the average resonance peak to be at 656 $\pm$ 1.11nm, with a full width at half maximum of 25 $\pm$ 1.33nm. More details about the fabrication of the plasmonic chip can be found in ref. [94].

In order to characterize the proposed plasmonic phase-sensitive detection platform, two different kinds of samples were fabricated. The first kind used microarrays of thin films of amorphous silica, as shown in Figures 3.1c) and d). The second kind used microarrays of a protein solution, as in Figure 3.1e). The protein experiments were carried out using a capillarity-based disposable microfluidic cartridge, shown in Figure 3.1f), which enables liquid manipulation

without pumps.

3.4 Optical response of the Au-NHA

The plasmonic Au-NHAs show the extraordinary transmission (EOT) phenomenon induced by two resonance coupling mechanisms in a classical asymmetric Fano-type spectral line profile [81, 95]. On the one hand, perpendicularly incident light generates in-plane surface plasmon polariton sub-radiant modes, according to Bragg's coupling condition through matching of the wave vector and the grating's momentum. On the other hand, dark modes couple to the subwavelength holes in the Au film and generate a bright radiant mode that scatters light into the free space. These destructive and constructive near-field interactions are strongly dispersive and manifest themselves in the far-field intensity spectrum as multiple dips and peaks that constitute different modes associated with either the supporting substrate or the sensing medium. A proper design of the Au-NHA chip will give a proper spectral separation between the different modes, which, in turn, will allow for sensing with different background media, such as air and water, as well as high sensitivity over a wide dynamic range. More details about the design and properties of the Au-NHA can be found in ref. [94].

Figure 3.2b) shows the numerically calculated intensity dispersion curve of the primary EOT sensing mode. The slope of this continuous EOT mode allows us to calculate the conventional bulk refractive index sensitivity

$$\sigma_{bulk} = \frac{\mathrm{d}\lambda_{EOT}}{\mathrm{d}n}, \tag{3.1}$$

where λ_{EOT} is the transmission peak wavelength and n is the refractive index of the sensing medium. The sensitivity in the visible-to-near-infrared range is σ_{bulk} =615nm per refractive index unit (RIU), which is in good agreement with literature values [81, 96].

Apart from intensity modulations, in the far-field, sharp phase transitions occur to the light that couples to the plasmonic surface [97]. Figure 3.2c) shows that the phase dispersion curve exhibits the same bulk sensitivity calculated on the intensity dispersion curve of Figure 3.2b). These phase transitions behave like temporal retardations at the resonance modes, which, in turn, can be detected with interferometric techniques, such as the LIM. Figure 3.2a) shows the expected optical response of an Au-NHA chip in the LIM. The orthogonally polarized pairs of rays (red and blue columns), traverse the plasmonic chip where
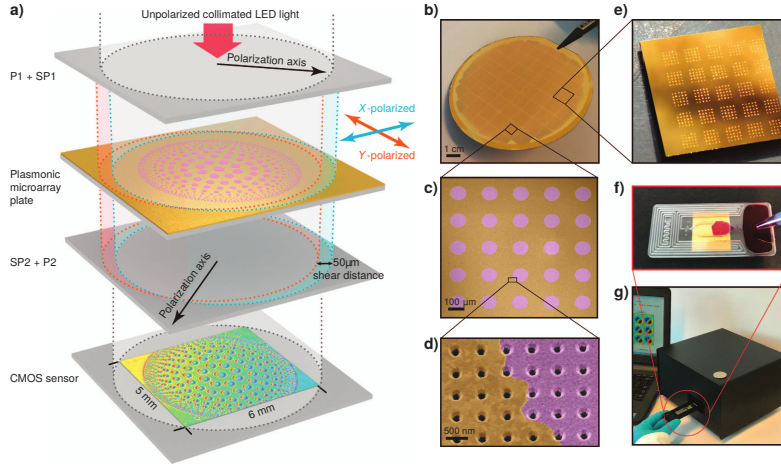
Figure 3.1: LIM and experimental setup. a) Collinear optical light-path configuration of the LIM setup. Collimated LED light beam is polarized (P1) and then sheared by a distance $S = 50\mu m$ by an SP (SP1). This generates quasi-spatially overlapped and orthogonally polarized light beams, which traverse the plasmonic chip and are subsequently recombined using a second SP (SP2) and interfered by a second polarizer (P2). Finally, the interferogram is imaged by the CMOS sensor. The image shown on the schematic CMOS sensor corresponds to the real measurement of a 10nm thin silica (SiO_2) pattern on a plasmonic chip. b) Photograph of a wafer comprising 1cm × 1cm plasmonic gold nanohole array (Au-NHA) chips fabricated using high-throughput, wafer-scale nanofabrication tools. c), d) Artificially colored scanning electron microscopy images of 10nm thin silica (purple color) microarrays on uniformly patterned plasmonic Au-NHAs. e) Photograph of a plasmonic chip with 200pL volume protein droplet microarrays formed using a low-volume liquid dispensing tool. f) Disposable capillarity-based microfluidic platform assembled on the plasmonic chip. g) Portable LIM operated through an interface running on an ordinary personal computer.

they are both intensity and phase modulated. As the Au-NHA plasmonic resonances are polarization-independent [98], the modulation functions vary only spatially depending on whether the material to be detected is present (defined as an ON region) or absent (defined as an OFF region). The redshift to the phase and transmission of the ON with respect to the OFF regions becomes evident in Figure 3.2d). In this system, the optical path difference is described as

$$\text{OPD} = \Delta\phi \frac{2\pi}{\lambda_{EOT}}, \tag{3.2}$$

where $\Delta\phi$ is the difference in phase ϕ in each pairs of orthogonally polarized rays.

In Figure 3.2a), the green zones of the OPD map correspond to the regions where the sheared beams go through identical optical paths, and, therefore, yield zero OPD after interference. The blue and red zones represent the expected double image signature of the LIM. These correspond to the regions where the beams are modulated by different phase functions (ϕ_{ON} and ϕ_{OFF}), leading to either positive or negative OPD values.

For transparent substrates, like the ones analyzed in chapter 2, phase differences depend only on the thickness of the material and the relative change to the surrounding medium in terms of refractive index. In this system, the phase differences are amplified by the plasmonic phase function, which results in an effective sensitivity increase.

Unlike the previous intensity-based plasmonic biosensors, which rely only on the spectral position of the EOT intensity peak, our methodology uses the OPD between the signal and reference beams. Figure 3.2e) shows the numerically computed phase contrast $\Delta\phi$ (left axis) and OPD (right axis) as functions of the refractive index difference ($\Delta n = n_{material} - n_{medium}$). The sensitivity of our system can also be analytically stated as

$$\sigma_{OPD} = \frac{\mathrm{d}OPD}{\mathrm{d}n} = \sigma_{bulk} \times \phi_{der} \times \frac{\lambda_{EOT}}{2\pi} \tag{3.3}$$

where $\phi_{der} = \mathrm{d}\phi/\mathrm{d}\lambda = 10$ [deg/nm] at the EOT peak, as indicated in Figure 3.2d). The OPD sensitivity can, therefore, be numerically estimated as 1.1×10^4nm/RIU over a dynamic range of 0.025 RIU, which is good for biosensing applications. The dynamic range of our system is mainly affected by the spectra of the plasmonic mode and the illumination source. More details on the plasmonic phase sensitivity can be found in ref. [94].

In the experiments, $\Delta\phi$ is extracted from ~ 30 interferograms recorded at different phase biases (introduced by SP1) after applying the PSI technique and the re-focusing algorithms as described in chapter 2. The fact that the samples in this case are not transparent is not a problem for obtaining the OPD with our PSI algorithm. Following eq. 2.1 in chapter 2, for the Au-NHA case, the electric field at an arbitrary point in the detection plane is

$$\vec{E} = \frac{1}{\sqrt{2}}e^{i\beta}[E_x e^{i(\alpha_x+\phi_x)}\hat{x} + E_y e^{i(\alpha_y+\phi_y)}\hat{y}], \qquad (3.4)$$

where β is an arbitrary initial phase for both polarizations, α_x and α_y are the phase differences due to the tilt of SP1, ϕ_x and ϕ_y the phase delays produced by the sample and E_x and E_y are the transmitted amplitudes to each of the two polarizations accordingly. After projection along the analyzer polarization (crossed polarization vector $\frac{\hat{x}-\hat{y}}{\sqrt{2}}$), and assuming that the tilt only affects the horizontal polarization (i.e. $\alpha_x = \alpha$ and $\alpha_y = 0$) and that ϕ_x-ϕ_y=ϕ, then the intensity will be

$$I(\alpha,\phi) = \frac{1}{4}(I_x + I_y - 2\sqrt{I_xI_y}\cos(\alpha+\phi)). \qquad (3.5)$$

where $I_x \propto |E_x|^2$ and $I_y \propto |E_y|^2$ are the intensities for each of the two beams after traversing the plasmonic chip. By integrating eq. 3.5 over complete periods of α, according to our PSI technique, the constant terms cancel out, returning the expected phase (ϕ) and an effective intensity ($\sqrt{I_xI_y}$).

3.5   Microarray detection

To demonstrate the capabilities of the LIM for microarray detection, large microarrays of silica layers with numerous thicknesses were identically patterned on two substrates, plasmonic Au-NHAs and transparent substrates, where the latter ones served as controls. OPD maps from microarrays with different silica thicknesses are shown in Figure 3.3a). For better clarity, only small representative regions from the full arrays are depicted. The overall contrast is calculated from the difference between the highest 5% and lowest 5% of the OPD values in a region (with constant size) around each spot. Therefore, the OPD contrast is expected to be about two times larger than the numerical OPD.

Figure 3.3b) shows the average OPD contrast data as a function of the silica thickness (bottom axis) and effective refractive index difference, Δn_{eff} (top
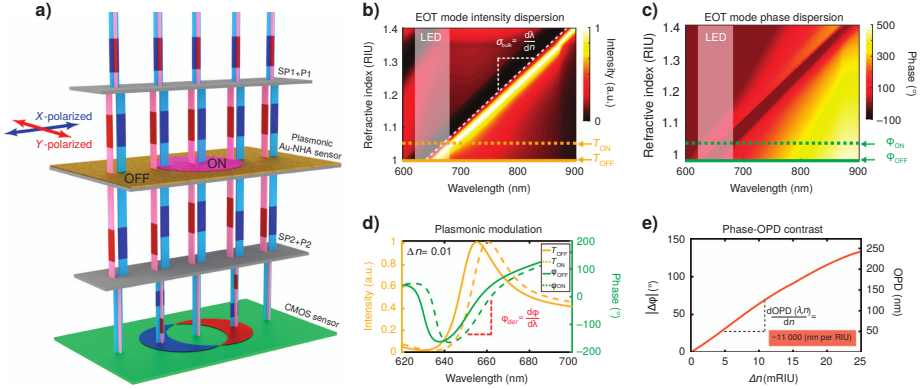
Figure 3.2: Phase interrogation principle of the LIM on plasmonic substrates. a) Trajectories of orthogonally polarized rays (red and blue columns), which are portions of the quasi-overlapped beams. Their intensity and phase are modulated after traversing the Au-NHA chip, due to the plasmonic mode coupling. The plasmonic phase and intensity modulation show spatial differences for the ON region (representing the microarray spot, in pink) with respect to the OFF region (bare plasmonic surface, in yellow). After recombination, the light beams generate interferograms captured by the CMOS sensor. b), c) Numerically computed transmission intensity and phase dispersion of the EOT mode, plotted as a function of the refractive index sensing medium. The LED spectrum, with peak wavelength $\lambda_{peak} = 656$nm, is also indicated on the plots. d) Representative intensity and phase modulation spectra associated with the ON and OFF regions with a refractive index difference Δn=0.01. The phase derivative ϕ_{der} corresponding to the EOT peak, which is a significant parameter in phase interrogation, is marked on the plot. e) Phase contrast $\Delta\phi$ and the corresponding OPD between the ON and OFF regions as a function of Δn are calculated at the EOT resonance wavelength λ_{EOT} of the bare chip. The refractometric LIM sensitivity can be numerically calculated from the slope of the curve.
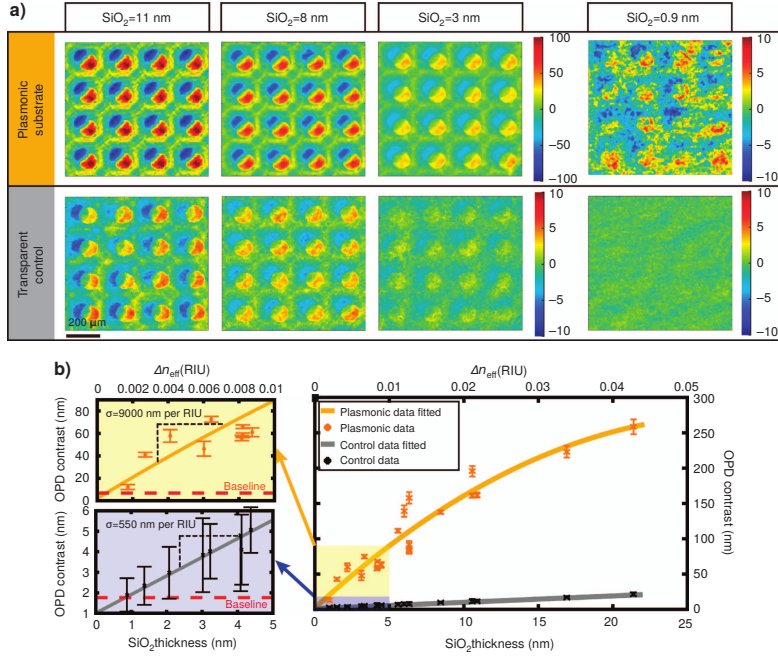
Figure 3.3: Silica microarray pattern detection with the LIM: comparison of plasmonic and transparent substrates. a) Color-coded OPD maps of various micro-arrayed silica (SiO$_2$) thicknesses, patterned identically on plasmonic and transparent control substrates. b) OPD contrast data (36 spots considered on each chip) statistically extracted from plasmonic and transparent microarray patterns are shown as a function of silica thickness, with the low thickness range magnified on the left. For convenience, the top axis indicates the effective refractive index units of the corresponding thin silica films. Baseline indicates the average OPD contrast of the bare substrate. Error bars correspond to the standard deviation over the 36 spots.

axis). The equivalence of Δn_{eff} for thin silica films has been calculated numerically, by relating the system responses with different thicknesses of the silica layers to the responses of the bulk media with different refractive indices [94]. In Figure 3.3b), each data point represents the average OPD contrast over 36 microarray elements and the baselines correspond to the same contrast calculations as for the regions without silica patterns.

We calculated the OPD sensitivities for silica thicknesses below 5nm from the slope of the fitted curve, as shown in Figure 3.3b) in the plots on the left.

The experimental sensitivity for the Au-NHA chip is $\sigma_{OPD_p} = 9000$nm/RIU and, for comparison, the equivalent sensitivity for the control samples is $\sigma_{OPD_c} = 550$nm/RIU (assuming the same ratio of silica layer thickness to bulk refractive index as for the Au-NHAs). From these numbers, we experimentally show that the plasmonic chips exhibit an OPD sensitivity $\sim 16\times$ higher than for the transparent control samples.

With the plasmonic phase modulation we have been able to detect atomically thin layers that cannot be resolved on transparent substrates, as demonstrated in Figure 3.3a) ($SiO_2 = 9$Å). In these experiments, we were limited by the minimum thickness of silica that can be deposited, this being 9Å. By interpolating the detection curve toward the background baseline, we have estimated the minimum detectable thickness to be 2.5Å.

By considering the background noise, i.e. the baseline (~ 4nm), together with the experimental sensitivity σ_{OPD_p}, we can estimate the minimum detectable RIU change $\sim 5 \times 10^{-4}$RIU. This value is about an order of magnitude better than in previous intensity-based measurements using Au-NHAs [98].

3.6 Biosensing

To demonstrate the capabilities of the LIM for biosensing, we show the detection of protein monolayer stacks on a microarray in dry and wet media. For this experiment, the illumination wavelengths were 656 and 870nm, since these correspond to the resonance peaks of the Au-NHA in air and in water, respectively.

Figure 3.4a) shows, schematically, the sequence of the monolayer stack formation and the OPD map of a representative part from the full microarray at each stage.

The first layer was formed by spotting droplets of 150pL volume from a protein A/G solution at a concentration of 0.5 mg/mL onto bare plasmonic chips. The remaining areas were then blocked with bovine serum albumin (BSA) at 1% v/v,

to form a thin layer around the protein spots, which prevented more proteins from binding. When the BSA covered the free surface of the chip, it decreased the topographic variation, consequently, the OPD values also decreased. Using the affinity of the protein A/G to the immunoglobulins (IgG), we tested the biosensing platform by adding two layers of IgGs, namely a mouse IgG (IgG1) and a goat anti-mouse IgG (IgG2), which binds to IgG1. For more details about reagents and procedures, see ref. [94]. The OPD maps in Figure 3.4a) indicate a contrast increase on the spots with protein A/G after the addition of each IgG layer.

Figure 3.4b) shows the spectra of the LEDs and the measured transmission spectra of the Au-NHA chips using a conventional spectrophotometer, coupled to an inverted microscope. The typical spectra associated with the bare and IgG2-coated chips in both wet and dry media are also depicted. The peak shift in a dry medium is $\sim$9nm, which is, as expected, larger than the one of $\sim$4nm for a wet medium. To a certain degree, this disparity is because the relative difference of the refractive index of the protein layers is greater in air than when surrounded by water. This effect can be observed in the OPD contrast data shown in the bar plots of Figure 3.4c), which show the average and the standard deviation after each layer formation. Each of the proteins has a different molecular weight (protein A/G $\sim$ 50 kDa, IgG $\sim$ 150 kDa) and, together with the concentration and chip sensitivity, this is reflected in the OPD contrast.

Further experiments were carried out by incubating the IgG1 microarrays with different concentrations of IgG2 buffer solution [94]. These preliminary results show that in this configuration, our method can detect a concentration of IgG2 as low as 500 ng/mL, which is an order of magnitude better than previous values for intensity-based biosensors using Au-NHAs [98]. Although the achieved limit of detection is significant, it can be further enhanced by means of better surface functionalization or additional labeling methods.

The Au-NHA substrates only enhance the phase signal of the material that is within the reach of the plasmonic surface fields ($<$ 100nm), as opposed to the transparent substrates, where the total volume between the SPs is equally probed. This emphasizes the importance of plasmonic phase enhancement for biosensing applications, where only proteins bound to the surface are to be detected, while the rest of the materials that are in the solution should not be.

These results already make it clear that the proposed platform, based on the LIM, is suited for multiplexed biosensing, with multiple steps and in different
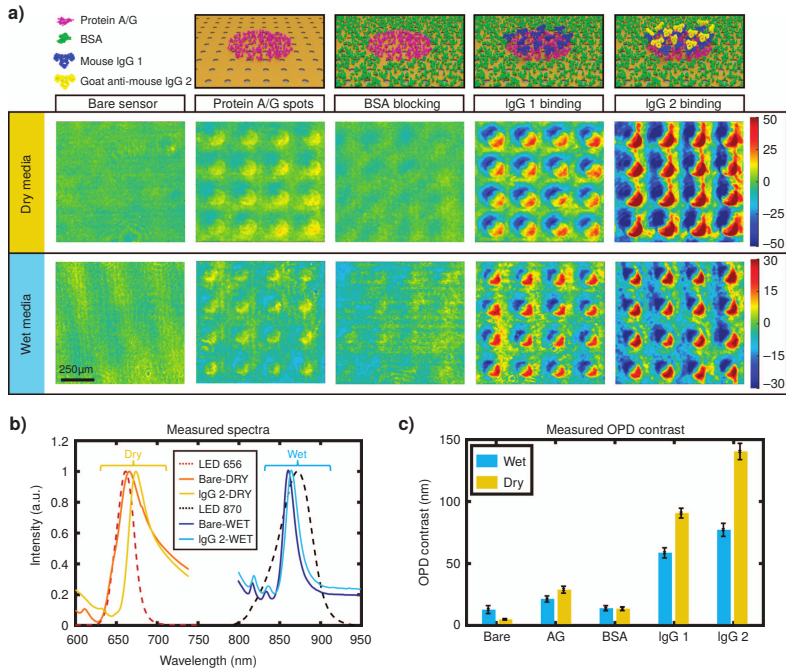
Figure 3.4: Protein microarray detection with the LIM, using the plasmonic phase interrogation scheme. a) Color-coded OPD maps of protein microarrays in dry and wet media are presented with corresponding protein stack information on the top row. b) Measured transmission spectra ON and OFF the IgG2 spots in both dry and wet media, as well as the LED illumination spectra. c) OPD contrast data (36 spots considered on each chip) statistically collected at each step of protein layer formation in dry and wet conditions. Error bars show standard deviation where N = 36.

kinds of media.

Hardware and software improvements, such as detectors with higher pixel density and improved image processing algorithms, could further reduce the lateral resolution down to the CMOS pixel size, i.e. $< 5\mu$m. This would potentially allow simultaneous access to over a million biomarkers, thus enabling an extraordinary multiplexing capability.

Conclusions

In this chapter, we proposed and demonstrated a novel platform for high-throughput and effective biosensing which exploits phase modulations enhanced by plasmonic effects in the LIM. We achieved high topographical sensitivity (atomic-scale) in this integrated nanophotonic system by properly designing the gold nanohole arrays (Au-NHAs) and their sharp transmission resonance. The exceptional multiplexing capabilities of the device can provide access to extremely large data sets of biomolecular information acquired from small quantities of biological samples. This would save time and reduce the costs of clinical testing. In summary, our platform demonstrates new ways of exploring the phase response of nanophotonic systems for sensing applications, as well as showing that it can have a significant impact in point of care (POC) rapid detection of life-threatening diseases.

Chapter 4

SPR + LIM: Towards phase-enhanced sensing for commercial plasmonic devices

4.1 Abstract

Sensors that are based on surface plasmon resonance (SPR) show a very high sensitivity to small changes in refractive index. This has been exploited for biomedical applications, e.g. for the evaluation of protein-antibody affinity, which, from a practical point of view, has made it one of the most successful plasmonic applications. Most of these sensors are based on the intensity variations caused by the interaction with the sensing medium, although it has been shown that the sensitivity of the sensor is greater when measuring the phase response. In this chapter, we show how the detection of refractive index changes in the LIM is enhanced by using SPR. Equivalently, we also show how the sensitivity of typical SPR techniques could be increased by using the LIM detection scheme.

4.2   Introduction

Sensors that exploit the surface plasmon resonance (SPR) and localized surface plasmon resonance (LSPR) demonstrate a high sensitivity to changes in the refractive index over a very small distance from the sensing surface, typically a fraction of the wavelength [99]. In general, SPR sensors show a greater sensitivity to measurements of the bulk refractive index than LSPR sensors, but due to the larger interaction distance of the SPR fields, LSPR and SPR show similar sensitivities for biosensing [100]. However, fabrication costs and methods, as well as simpler functionalization techniques, are in favor of SPR sensors. These attributes have boosted SPR as a technology that is well established and commercially available through many companies that have emerged over the decades, with Biacore AB being the first to commercialize the technology and the one with the strongest presence in scientific research [101, 102].

A proper surface chemistry of the sensor allows for selective binding of a desired material to the surface. If the binding of this material produces a local change in the refractive index, this will in turn affect the resonance conditions and can be detected as, for example, changes in the transmitted or reflected light. In this way, several techniques based on SPR have been reported for the detection of small molecules, proteins, nucleic acids, viruses, bacteria and other materials [75, 102–105].

Many of the commercial SPR systems, like that of Biacore, belong to the group of intensity-based spectroscopic SPR sensors where the response over the angular or wavelength spectrum of the incident light carries information about the medium to be analyzed, reaching a limit of detection (LOD) of 10^{-7} refractive index units (RIU), similar to that of other sensors based on the intensity response of [75]. This sensitivity limit has been surpassed by a different sensing approach, where the sharp phase jumps at the resonance are measured [89], showing an increase in sensitivity towards the classical intensity-based measurements and leading to an LOD of 10^{-8} RIU [106].

In Figure 4.1, we can observe the spectroscopic behavior that is expected for the reflected intensity (reflection) and phase in a classical SPR configuration when in contact with two liquids with slightly different refractive indices. One can see that the phase response shows a steep slope at the respective resonance wavelengths, which ultimately leads to a significant increase in the difference in the signal of the sensing liquids.

Despite the important increase in sensitivity, phase detection schemes have not been exploited to the same extent as their intensity-based counterparts, in part due to the fact that sophisticated equipment and optical setups are usually
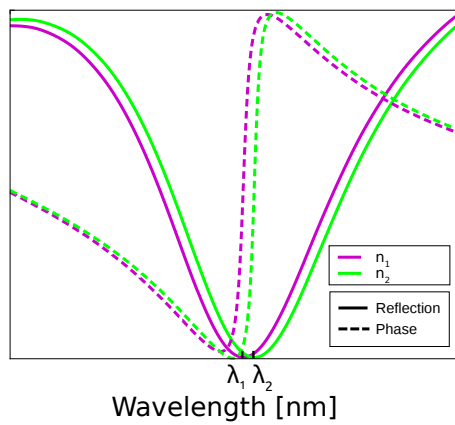
Figure 4.1: Expected behavior close to the resonance condition for different wavelengths in a classical optical SPR setup with a P polarized beam impinging at a fixed angle. The solid and dashed lines represent,respectively, the reflected intensity (reflection) and phase delays that modify the reflected beam. The colors indicate the responses when two different media with bulk refractive indices n_1 and n_2 ($n_2 > n_1$) are in contact with the sensing surface, showing a displacement of the resonance wavelength from λ_1 to λ_2. The curves have been normalized to allow an easy comparison.

needed.

The main objective of this chapter is to demonstrate that the LIM can be used as a simple additional tool in classical intensity-based SPR systems, enhancing their sensitivity using a compact and stable setup. Here, we compare the intensity and phase detection schemes in our system with those of intensity-based SPR imaging with a similar non-interferometric lens-free configuration.

4.3   Experimental setup and optical response

An ideal experimental setup for comparing the sensitivity in each scheme would involve an SPR chip with spatial variations containing active sites, whose response could be controlled continuously. An approximation of this was demonstrated in chapter 3 with the protein/antibody layer experiment. However, the thickness in this case cannot be fully controlled or easily reversed to reproduce the same conditions in each scheme.

The approach used for this chapter is an SPR chip with fixed surface variations, showing different plasmonic responses. The chip is immersed in different liquids with controlled refractive indices, which will change the resonance conditions. By measuring at different wavelengths, we can probe a broad region of the responses and evaluate the performance of the technique.

Figure 4.2a) depicts our experimental setup and the trajectory of two arbitrary rays (from a wide collimated beam) that are combined and interfered just before being detected. A tunable laser (SuperK COMPACT with a tunable filter VARIA from NKT Photonics) emits light at a given wavelength (λ) in the range from 500 to 800nm and with a controlled bandwidth of $\sim$5nm. The light is emitted from a fiber and collimated with a parabolic reflective collimator (not shown in the image). The collimated beam traverses a linear polarizer (P1) oriented either at S or P polarization (pol.). After being reflected inside the SPR prism, the beam passes through the Savart plate (SP) which produces two parallel and quasi-overlapped copies of the original beam, separated by a distance $S = 50\mu$m. The displacement of the two beams is parallel to the P pol. The resulting beams have orthogonal polarizations ($\pm 45^{o}$ relative to the P pol.), as determined by the axes of the SP. The SP can be tilted in order to produce a relative phase delay α between the two beams. The combined beam after the SP goes through a linear polarizer (P2), parallel to the P pol., and is detected by a CMOS image sensor. In this case, the distance from the center of the reflective surface to the dector is 34mm.
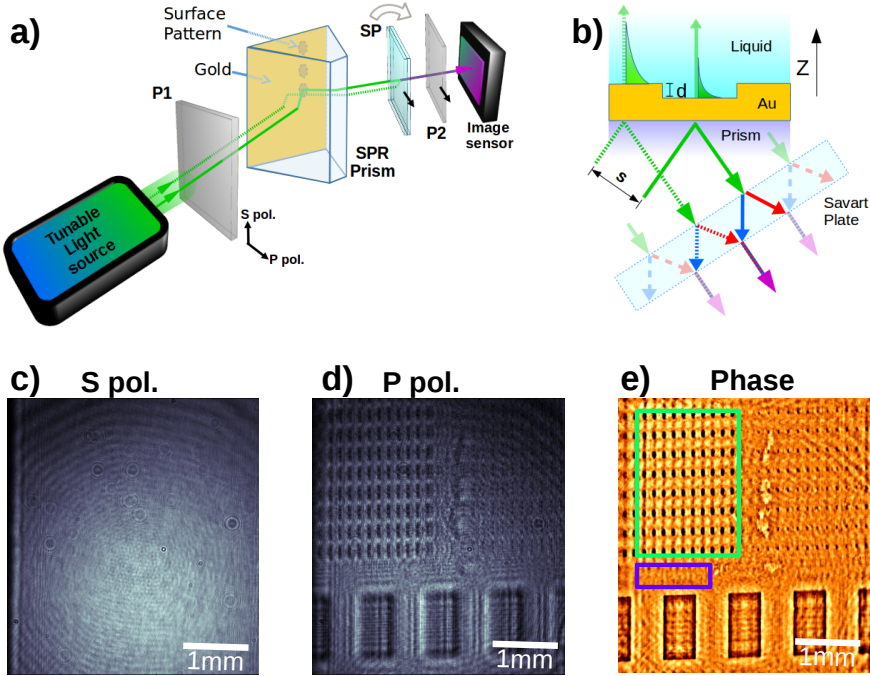
Figure 4.2: a) Experimental setup consisting of a tunable light source, linear polarizers P1 and P2, an SPR prism with a patterned Au-coated sensing surface, a Savart plate (SP) and a CMOS image sensor array (ISA). An arbitrary pair of rays from the full beam shows the reflection and re-combination process through the components. b) Detail of the SPR prism surface and ray trajectories. The gold coating on the prism, with approximate thickness of 50nm, is in contact with a liquid and shows a carved pattern with depth $d \sim 9nm$. Two arbitrary rays separated by a distance S (the shear distance) show the evanescent waves generated on the back side of the prism. The rays are split into two by the SP. Each ray will overlap and be allowed to interfere with the split ray from a neighboring point from a distance S. c) and d) Intensity captures obtained from the ISA when P1 is set at S or P pols., respectively, for a wavelength $\lambda = 650nm$. e) Phase image of the sample after processing 30 interferograms with both polarizations. The green and purple rectangles represent the areas used for the statistical analysis.

Since these SPR experiments show a high polarization dependence, we have eliminated the SP that goes before the sample, which is present in the other LIM setups as SP1. The reason for this modification is that even small imperfections or misalignments in SP1 would lead to detectable errors due to polarization contamination. This modification does not alter the LIM detection scheme since, as demonstrated in Figure 4.2b), any two rays from the original beam that are separated by a distance equal to the shear will each be split by the SP and their corresponding copies will later interfere with the neighboring beam. The drawback of not having SP1 is that we increase the interferometric sensing volume. This means that every inhomogeneity that occurs before SP (e.g. dust particles in P1 or inhomogeneities in the illumination beam) will produce a detectable interferometric signal. This implies that this external noise is not canceled by the system itself (as in the case of the LIM) but, instead, we can subtract this noise using the reference measurement.

For our experiments the chips were commercial SPR prisms (SPRi-Biochip, Horiba Scientific), which are ideal for SPR imaging, using the Kretschmann configuration and light in the red to near-infrared part of the spectrum. Typically, the sensing surface is functionalized in order to build arrays of binding sites for the analytes that are to be detected. The exact composition of these prisms is not officially reported, but some sources report that they consist of a prism of high refractive index glass (SF-10) with a 5nm chromium layer covered by a 50nm gold layer [107].
In our case, the SPR chip was designed to have ultra-thin layers of 5nm of silica, forming arrays of dots with varying diameters and separation distances. However, the same fabrication procedure used for making the silica samples in chapter 2 and the patterning of the gold nanohole array (Au-NHA) chips in chapter 3, in this case stripped-off the silica and part of the gold, leaving 9nm to 10nm-deep holes on the sensing surface (measured with an atomic force microscope). We assume that the adhesion of the gold on the commercial prism is different to the in-house fabricated surfaces, probably due to a different coating process. Nevertheless, the desired effect can still be achieved since small variations in the thickness of the Au layer change the plasmonic response in terms of reflection and phase [99, 108]. In general, if we start from the optimal Au thickness, a small thickness change will make the absorption dip shallower and broader and the phase jump will become less steep, and, beyond a certain thickness variation, the phase jumps can even flip down [108]. The resonance peak position is not significantly affected.

Since there are still unknown parameters (e.g. the absolute thickness of the Au layer after the fabrication process) which lead to different behaviors, we simply consider this as an SPR chip that modulates a reflected P polarized electric field E_0 and write it as

$$E(d) = E_0 \sqrt{R(d)} e^{i\phi(d)}, \tag{4.1}$$

with R being the reflection and ϕ the corresponding phase delay induced by the plasmon interaction at the region with a surface variation d (for the flat regions, without arrays, $d = 0$). Both functions, R and ϕ, depend on λ and the refractive index n of the sensing liquid. Following a similar analysis to the one leading to eq. 3.5 in chapter 3, we consider the electric fields E_u and E_v, which correspond to the sheared beams, with orthogonal polarizations u and v. After the PSI technique, we measure an effective phase $\phi = \phi(d_u) - \phi(d_v)$ and reflection $R = \sqrt{R(d_u)R(d_v)}$, where d_u and d_v depend on the region where the electric fields are reflected.

Figure 4.2b) shows a close-up of the prism, demonstrating a carved hole on the Au surface, which is in contact with the sensing liquid. Two rays that were selected to be at a distance S from each other are depicted together with the evanescent waves that they generate on the Au-liquid interface. The two rays are split into two orthogonally polarized copies by the SP. At the exit of the SP, each copy of the ray will be combined with the split ray from a neighboring point, separated by a distance $\pm S$, and will interfere with it after P2.

The prism with de-ionized (Milli-Q) water at 22.5^oC as the sensing liquid was aligned to show the minimum of intensity at $\lambda \approx 700$nm, since it is a favorable region for phase sensing [89]. The internal angle of incidence has been estimated to be 63°, based on the the geometrical deformation of the patterns in the captured images. In Figures 4.2c) and d), we show the raw intensity captures as obtained from the ISA when P1 is parallel to either the S pol. or P pol., respectively. It becomes clear that the pattern, visible in d), only appears under the P pol., due to the plasmonic effect. In Figure 4.2e), we see the measured phase of the sample after analyzing 30 interferograms with controlled SP tilts, using the same PSI and reconstruction algorithms from chapter 2. In this case, we have measured the sample with the P pol., while using as a reference a measurement with the S pol., in order to compensate for the noise coming from the system. In Figure 4.2e), a green rectangle depicts the boundary of the region containing the array of circular holes with 75μm diameter and depth $d \approx 9$nm, and the purple rectangle shows the flat region. Both were used for the statistical analysis.

In order to induce controlled shifts in the resonance conditions of the chip, we used liquids with concentrations of 0.0%, 0.5%, 1.0% and 2.0% (w/w) of glycerol in water, which have the following refractive indices [109]:

Glycerol Concentration (w/w)	0.0%	0.5%	1.0%	2.0%
Refractive index	1.33303	1.33359	1.33416	1.33530

The wavelengths for these values are not specified and the temperature is slightly different to the temperature in our measurements. However, a comparison with the values of the refractive index of pure water [110] allows us to approximate the offset in the refractive index for the range of liquid concentrations and wavelengths in our experiment as a bias in the order of 10^{-4}RIU. This, in any case, is smaller than the difference in n between the liquids.

In Figure 4.3, we show the measured OPD maps of the SPR chip for 0.0% glycerol (pure water) and the difference in OPD when compared with the 2.0% sample. The maps are measured with wavelengths that are far from (500nm), before (675nm) and immediately after (705nm) the resonance. Even though the values are lower, we are still able to observe the pattern at wavelengths far from the resonance, which indicates that the difference in the phase response between the patterned and the flat regions is high. However, the sensitivity of the chip for the different wavelengths becomes more evident when analyzing the change in the response for different bulk refractive indices. Here, we can clearly see that the performance of the chip is low when λ is very far from the resonance, since the signal from the pattern is at the same level as the background noise (OPD~1nm).

The difference in the response, due to a change in the refractive index, increases as we probe closer to the resonance. This can be observed in the range of values for the difference in OPD, as well as in a higher contrast and a lower background noise which, ultimately, will lead to a better signal to noise ratio (SNR). An increase in the SNR is an indication of a real sensitivity enhancement, discarding a false magnification of the signal together with the noise, which could have been present, since the regions with higher phase sensitivity are precisely the regions where we detect the lowest intensity in the interferograms.

The maximum OPD values obtained for the array with the plasmonic configuration range between 190 and 200nm for wavelengths between 705 and 710nm (depending on the liquid). In order to compare the sensitivity gained with the SPR effect, we measured directly the Au surface in air with a LIM that works in perpendicular reflection. This gave OPD values of between 18 and 20nm, which

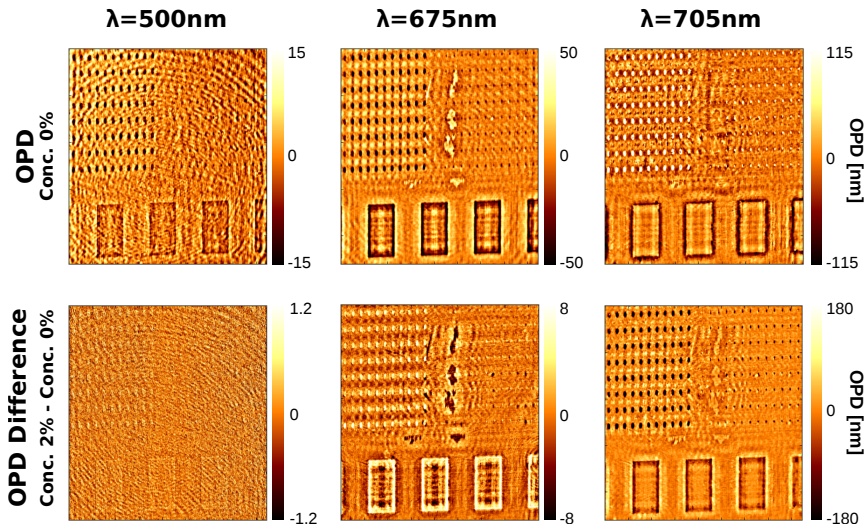Figure 4.3: Top row: Measured OPD of the patterned gold surface via SPR with pure water, for different wavelengths. Bottom row: difference with respect to pure water in the measured OPD when using a solution of 2.0% glycerol in water (w/w). For a better qualitative comparison of the sensitivities, in all cases the OPD axis is proportional to the standard deviation (not maximum and minimum) of the values.

are in good agreement with the expected value of $OPD = 2d \times n_{air} = 18$nm, where $n_{air} = 1.0$ and $2d$ is the additional path for the beams reflected inside the holes. The SPR chip increases the measured OPD by $10\times$ with respect to the OPD measured with the standard LIM in reflection. However, when we calculate the difference in OPD for the cases with 0% and 0.5% concentrations of glycerol, for the SPR configuration we get a value of 200nm at $\lambda = 705nm$. If we could perform the same comparative experiment with the standard LIM, without reflection and without plasmonics, we would expect a difference of

$$\Delta OPD = d \times (n_{0.5\%} - n_{0\%}) = 0.01nm, \tag{4.2}$$

where $n_{0\%}$ and $n_{0.5\%}$ are the refractive indices for the liquids with 0% and 0.5% glycerol, respectively. This result means that by using the SPR chip, we increase the sensitivity of the LIM about 100 times and that we get a differential OPD signal magnification of 2×10^4 for refractive index variations. Further experiments have to be carried out to confirm the same enhancement in the limit of detection for biomarkers, since SPR techniques are known to have less sensitivity for the detection of thin layers compared to bulk refractive index [100].

4.4   Sensitivity enhancement analysis

We have demonstrated that the implementation of an SPR chip can enhance the performance of the LIM, but could the LIM enhance the detection of classic intensity-based SPR sensors as well?
To answer this question, we modified the setup of the LIM in order to obtain a non-interferometric classic lens-free microscope (CLM), which is the same setup as in Figure 4.2a) after discarding the SP and the P2. The procedure for the measurements with the CLM is essentially the same as the one described in chapter 2:

- The CMOS takes 30 images with the same exposure time as with the LIM, to ensure similar noise conditions. The images are averaged.

- Since the phase-shifting interferometric (PSI) technique cannot be implemented, the complex electric field is calculated from the square root of the detected intensity.

- The electric field is propagated numerically to the sample plane, resulting in the refocused intensity and phase maps. The refocused maps at

the negative sample distances are averaged with the ones at the positive sample distances, this time showing no displacement in the features. The phase is converted to OPD for an easier comparison.

- Each measurement is made with P1 at P pol. and the system noise is decreased with a reference measurement with P1 at S pol. (where the plasmonic effect is not excited).

The measurements were carried out for 17 wavelengths ranging from 690 to 715nm in steps of 2nm (1nm in the resonance region, from 700 to 706nm, due to faster variations), using liquids with 0%, 0.5% and 1.0% glycerol, in both setups, LIM and CLM. The minimum intensity for the SPR chip with 0% glycerol was found at $\lambda =$702nm.

Because of the large phase enhancement from the SPR chip, a CLM can also retrieve relevant phase information, due to diffraction. Standard non-interferometric lens-based SPR imaging systems are not able to detect these phase signals, only those related to absorption.

We analyzed the OPD (phase) and reflection (amplitude) responses for both the array of dots (signal) and the flat region (noise). We assumed that the flat region carries only information regarding the system noise; however, an analysis with an optical profiler (SENSOFAR S neox Optical Profiler) also revealed minor surface variations of $\sim 0.5nm$ over a distance S.

Every dot in the array was analyzed by calculating the median of the values in a rectangular cell, fully contained inside the dot and of constant size for all the dots. From this set of values we again calculated the median, i.e. the $Signal_{median}$. Similarly, the flat region was divided into small cells (with the same sizes as the ones for the dots), and from each cell we computed the median and the standard deviation of its values. The median values of these two sets of values are the $Noise_{median}$ and $Noise_{std}$, respectively. In these cases, the median is a better parameter than the average, since it is less affected by noise and out-layer values, therefore providing the most representative values from the set.

Depending on the nature of the signal, one may find several definitions of the SNR formula. In our case, since the average of our noise can be zero (especially for the OPD or differential values), we define it as

$$\text{SNR} = \left| \frac{Signal_{median} - Noise_{median}}{Noise_{std}} \right|. \tag{4.3}$$

The numerator in eq. 4.3 contains the information about the contrast of the dots, relative to the background. The denominator evaluates how this contrast compares with the noise inside the same cell. If the SNR < 1, we are in principle unable to differentiate the signal of the dots from the background noise.

The graphs in Figure 4.4 (Figure 4.5) represent the data from the signal and the SNR of the reflection (OPD) and of the difference in the reflection (OPD) when compared to the case with 0% glycerol. For the differential plots, the statistical analysis is carried out after the subtraction of the maps.
A simple way to interpret the plots in Figures 4.4 and 4.5 is as follows. The signal plots (top rows) indicate how well we can distinguish one refractive index from another, either by measuring a spectral shift in the signal (left plot) or by measuring an increase in the differential signal at a fixed λ (right plot). Their respective SNR plots indicate how good a measurement is and can suggest which of the detection schemes, LIM or classic SPR, is better in each scenario.
Even though this SPR chip could have a sub-optimal response, due to the different thicknesses of the Au layer, key information can still be extracted from the different measurements.

Reflection measurements

- The reflection signal shows, with both schemes, the expected dip and red-shift in the resonance for higher concentrations (larger n).

- Based on the SNR, differential reflection measurements only show an advantage, towards the spectral shift analysis, for wavelengths after the resonance, where non-differential measurements show a significant drop in SNR.

- In general, the LIM and classic schemes perform similarly for measurements of the reflection signal close to the resonance.

OPD measurements

- With both schemes, the OPD signal resembles the expected phase response of SPR, including the red-shift of the curves for larger n.

- The SNR associated with the OPD signal is in general high and, before the resonance, is similar for both schemes. After the resonance, the LIM shows up to 4 times better SNR.

- The OPD SNR plots show a sharp drop at the resonance wavelength (the classic scheme shows an additional offset in λ), related to the steep slope of the signal curves. The resulting SNR dip in the case of the LIM is clearly narrower than in the classic scheme; moreover, it is significantly narrower than the dip in the reflection signal.

- Differential measurements in OPD prove to have a positive impact on both the signal and the SNR curves. For the LIM, the OPD difference values are up to 4 times larger than the classic scheme, with peak values that are up to 3 times better.

- A direct comparison shows that the OPD SNR with the LIM is 6 times better than the reflection SNR of the classic scheme.

These results suggest that the LIM can increase the already high sensitivity of classic intensity-based SPR detection systems.
In classical intensity-based SPR detection, limits in the sensitivity have been overcome by developing algorithms in order to find, with better precision, the minimum of the resonance dip [103, 111]. An analysis of the narrow OPD SNR dips in the LIM, instead of the reflection (intensity) dips, could also improve the determination of small changes in the refractive index.

By assuming a linear relation between small differences in the refractive index and the OPD difference SNR, we can estimate a LOD with the LIM of 3×10^{-5} RIU, for changes in the bulk refractive index. Although the minimum LOD reported in literature is as low as 10^{-8} RIU [106], for that kind of sensitivity the setups involve more sophisticated equipment, stabilized light sources, narrower bandwidths and temperature control, which, nevertheless, could also be used with the LIM.
Our estimation of the LOD would make it one order of magnitude better than the LOD in chapter 3 for refractive index sensing. However, we cannot directly translate this result into a better sensitivity for biolayer detection due to the differences in the interaction with thin layers of SPR and Au-NHA chips [100]. Further experiments are needed in this respect.

It should be pointed out that these experiments were performed with a LIM configuration without the SP1 and outside optimal sensing conditions, since the registered OPD signals were about 20 times higher than the ones for which the LIM was designed. By introducing an SP1 and an optimized SPR chip with a lower base response, as well as working in the regime of small refractive index

Figure 4.4: LIM (solid lines) and CLM (dashed lines) data plots of the reflection in the patterned array for wavelengths around the resonance conditions with a solution mixture of glycerol in water at 0.0% (blue), 0.5% (green) and 1.0% (red) by weight. Top left: Reflection of the spots in the array. Top right: Difference in the reflection of the spots with respect to the 0% glycerol case. Bottom left: SNR of the reflection of the spots in the array. Bottom right: SNR of the difference in the reflection of the spots with respect to the 0% glycerol case.
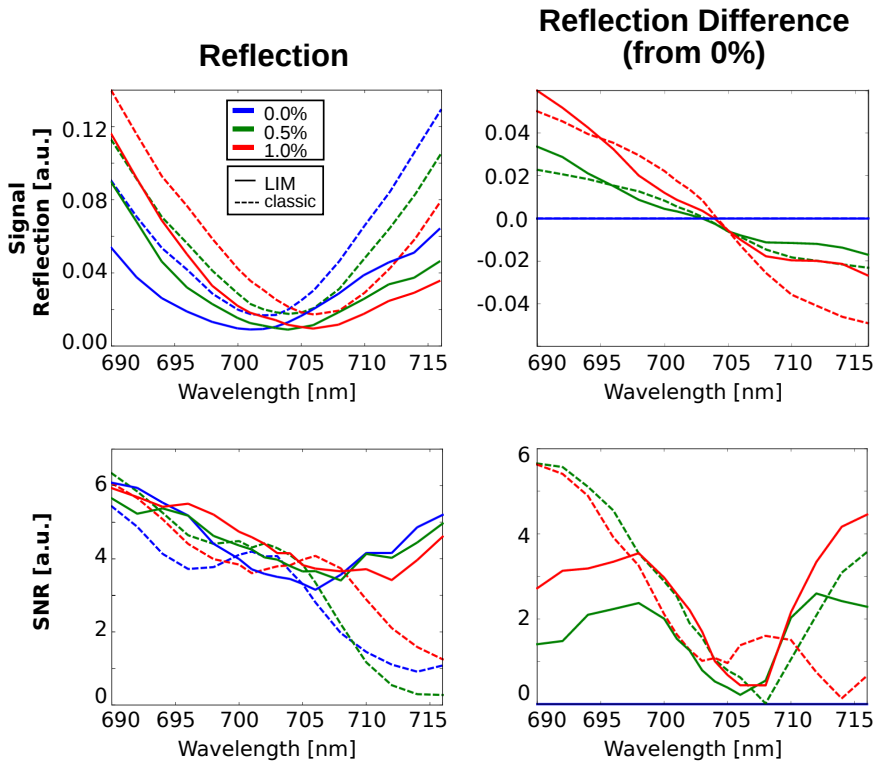
Figure 4.5: LIM (solid lines) and CLM (dashed lines) data plots of the OPD in the patterned array for wavelengths around the resonance conditions with a solution mixture of glycerol in water at 0.0% (blue), 0.5% (green) and 1.0% (red) by weight. Top left: OPD of the spots in the array. Top right: Difference in the OPD of the spots with respect to the 0% glycerol case. Bottom left: SNR of the OPD of the spots in the array. Bottom right: SNR of the difference in the OPD of the spots with respect to the 0% glycerol case.

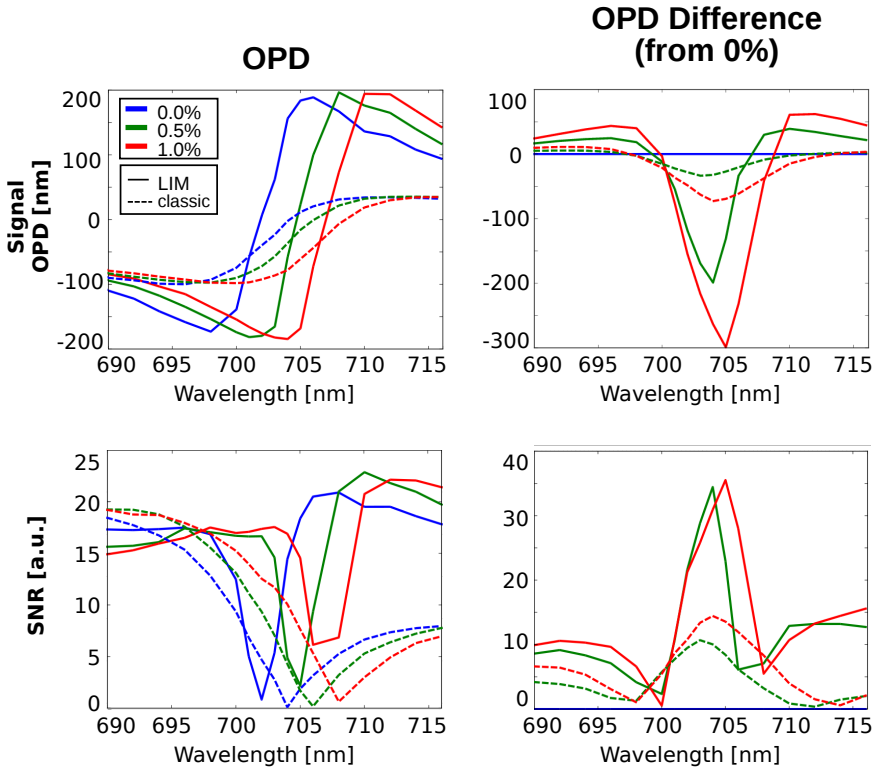changes, we should be able to improve the SNR and LOD with the LIM.

4.5   Conclusions

In this chapter, we have demonstrated that the phase sensing scheme of the LIM can be enhanced by SPR. The LIM allows simultaneous measurement of the intensity and phase modulations, for different wavelengths, as expected from the plasmonic interaction of the sensing surface with the medium of a given refractive index. The sensitivity of the LIM is improved by 2 orders of magnitude and signal amplifications of up to 4 orders of magnitude were observed.

Moreover, the results suggest that the sensitivity of intensity-based SPR sensors could be improved by at least a factor of 4 with the LIM.

The LOD for changes in the bulk refractive index with the LIM was estimated as 3×10^{-5} RIU, which can be improved with some modifications to the system and with more precise equipment, which has already been used to achieve lower LOD in literature.

Conclusions

In this thesis, a new lens-free interferometric microscope (LIM) has been developed and tested for detecting transparent materials and biomarkers, also in combination with plasmonic enhancement. The LIM is simple, robust and made of inexpensive components such as linear polarizers, LEDs and birefringent elements.
Its main characteristics are:

- The balanced optical path configuration of the LIM allows the use of almost any type of light source, including those with a low coherence length, for instance, LEDs.

- The lateral resolution of the reconstructed images is $\sim 35\mu$m, which is sufficient for microarray applications and, in the future, can be improved with simple changes in the hardware.

- The field of view of the reconstructed images is larger than 20mm^2 and can be increased with a larger image sensor array.

- The sensing volume is defined by the region between the two Savart plates in the setup. The distance that can be refocused after measurements, without losing lateral resolution, is around 30mm.

- The resolution for the optical path differences (OPD) is 1nm, allowing for the detection of microarrays of protein monolayers like bovine serum albumin and its corresponding antibody.

- New phase-shifting and image reconstruction algorithms have been developed to retrieve the signal from the recorded interferograms.

On the one hand, the sensitivity of the LIM can be further enhanced by plasmonic chips, namely a gold nanohole array (Au-NHA) substrate and a commercial surface plasmon resonance (SPR) prism. On the other hand, the sensitivity of these chips can also be enhanced by the phase detection scheme of the LIM. More specifically by combining the LIM with the Au-NHA chips, we have demonstrated that:

- The Au-NHA chips are polarization independent and stable against misalignments, making them useful for point of care (POC) applications.

- The Au-NHAs excite sharp localized SPR (LSPR) modes that were probed with light at wavelengths of 656 and 870nm when in contact with air and water, respectively.

- Phase detection at the resonance wavelengths enhances the sensitivity of the AuNHA chips, with an estimated limit of detection (LOD) for differences in the refractive index $\sim 5 \times 10^{-4}$ refractive index units (RIU). The estimated LOD for concentrations of inmunoglobulin (IgG) is as low as 500 ng/mL. Both LODs are one order of magnitude better than the previously reported intensity-based results.

- The estimated LOD for silica microarrays is a thickness of 0.25nm, which is an order of magnitude better than that without the plasmonic substrate.

As for the combination of LIM with commercially available SPR chips, we have shown that:

- The plasmonic signal from the SPR chip is highly polarization dependent. For a specific alignment, the effect takes place at wavelengths between 500 and 800nm, with the resonance at 702nm, when in contact with pure water.

- Solutions of glycerol in water were used to investigate the sensitivity in terms of changes in the bulk refractive index, with an estimated LOD of 3×10^{-5}RIU, which would prove to be an order of magnitude better than the bulk sensitivity of the Au-NHA. Further experiments need to be carried out in the case of protein detection.

- A direct comparison with a non-interferometric lens-free microscope suggests that the LIM could improve the sensitivity of commercial intensity-based SPR sensors by, at least, a factor of 4.

The LIM has shown that the sensitivity of lens-free microscopes could be improved with interferometric techniques. This thesis also shows that the LIM is fully compatible with plasmonic techniques, either with cutting edge plasmonic substrates or with well-established commercial chips. A combination of these techniques can reach sensitivity levels that are much higher than any of them individually.

Outcome of the RAIS project

The work contained in this thesis was fundamental for the success of the EU funded RAIS project concluded in March 2018, its main results being:

- A POC platform was developed using the LIM and Au-NHA chips for label-free detection of Sepsis biomarkers in 30 minutes. The measurements in the reader only took 2 minutes, with the remaining time needed to ensure a proper binding of the biomarkers.

- The POC prototypes were transported to several locations in different countries, without affecting their performance, showing the robustness of the device.

- Biomarkers including C-reactive protein, procalcitonin and Escherichia coli were analyzed with the platform. In the case of Escherichia coli, the most common bacterial pathogen causing Sepsis, a remarkable LOD as low as 1 single unit was achieved.

- Measurements of the plasma from real Sepsis patients were carried out together with the Catalan Institute of Nanoscience and Nanotechnology at the Vall d'Hebron Barcelona Hospital Campus. The results obtained with the POC platform allowed for the rapid detection of Escherichia coli, with the ability to discriminate between healthy and systemic inflammatory response syndrome (SIRS) patients and those with Sepsis.

These results show that the POC platform, based on the lens-free interferometric microscope developed in this thesis, has a high potential to make an impact in the fast diagnosis of dangerous infection diseases.

Outlook

The results that have been demonstrated in this thesis show that the LIM, by itself, is a powerful tool that allows the detection of highly transparent and

thin materials and that it is possible to improve its sensitivity by combining it with other techniques. There are, however, some aspects that should be further developed.

For instance, the spatial resolution and measuring time of the LIM can still be improved, in order to allow a higher density of sensing sites and the study of binding kinetics, respectively. This could be achieved by selecting new hardware, like a faster image sensor and processing unit, together with proper adjustments to the algorithms.

A bit more challenging is to further increase the sensitivity of the platform, which would allow for the detection of biomarkers with a lower molecular weight. The use of plasmonic techniques in combination with the LIM has proved to be very effective and more research needs to be done in this field, for example, by investigating the sensitivity enhancement produced by the use of new plate structures including metal plasmonics and dielectric Mie resonances.

Finally, the preliminary results of the combination of LIM and SPR show that this has a great potential for a sensitivity enhancement and further research is necessary.

Bibliography

[1] M. G. L. Gustafsson. Surpassing the lateral resolution limit by a factor of two using structured illumination microscopy. *Journal of Microscopy*, 198(2):82–87, 2000.

[2] Lothar Schermelleh, Rainer Heintzmann, and Heinrich Leonhardt. A guide to super-resolution fluorescence microscopy. *The Journal of Cell Biology*, 190(2):165–175, 2010.

[3] Alon Greenbaum, Wei Luo, Ting-Wei Su, Zoltan Gorocs, Liang Xue, Serhan O Isikman, Ahmet F Coskun, Onur Mudanyali, and Aydogan Ozcan. Imaging without lenses: achievements and remaining challenges of widefield on-chip microscopy. *Nat Meth*, 9(9):889–895, Sep 2012.

[4] John N. Nkengasong, Peter Nsubuga, Okey Nwanyanwu, Guy-Michel Gershy-Damet, Giorgio Roscigno, Marc Bulterys, Barry Schoub, Kevin M. DeCock, and Deborah Birx. Laboratory systems and services are critical in global health: Time to end the neglect? *American Journal of Clinical Pathology*, 134(3):368–373, 2010.

[5] David McCoy, Sudeep Chand, and Devi Sridhar. Global health funding: how much, where it comes from and where it goes. *Health Policy and Planning*, 24(6):407–417, 2009.

[6] Ilesh V. Jani and Trevor F. Peter. How point-of-care testing could drive innovation in global health. *New England Journal of Medicine*, 368(24):2319–2324, 2013. PMID: 23758238.

[7] Samiksha Nayak, Nicole R Blumenfeld, Tassaneewan Laksanasopin, and Samuel K Sia. Point-of-care diagnostics: Recent developments in a connected age. *Analytical chemistry*, 89(1):102–123, 2016.

[8] Paul Yager, Gonzalo J Domingo, and John Gerdes. Point-of-care diagnostics for global health. *Annu. Rev. Biomed. Eng.*, 10:107–144, 2008.

[9] Hongying Zhu, Serhan O Isikman, Onur Mudanyali, Alon Greenbaum, and Aydogan Ozcan. Optical imaging techniques for point-of-care diagnostics. *Lab on a Chip*, 13(1):51–67, 2013.

[10] Sandeep Kumar Vashist, Peter B Luppa, Leslie Y Yeo, Aydogan Ozcan, and John HT Luong. Emerging technologies for next-generation point-of-care testing. *Trends in biotechnology*, 33(11):692–705, 2015.

[11] Onur Mudanyali, Derek Tseng, Chulwoo Oh, Serhan O. Isikman, Ikbal Sencan, Waheb Bishara, Cetin Oztoprak, Sungkyu Seo, Bahar Khademhosseini, and Aydogan Ozcan. Compact, light-weight and cost-effective microscope based on lensless incoherent holography for telemedicine applications. *Lab Chip*, 10:1417–1428, 2010.

[12] Arif E. Cetin, Ahmet F. Coskun, Betty C. Galarreta, Min Huang, David Herman, Aydogan Ozcan, and Hatice Altug. Handheld high-throughput plasmonic biosensor using computational on-chip imaging. *Light: Science & Applications*, 3(1):e122, jan 2014.

[13] http://www.rais-project.eu, 2018 (accessed June, 2018).

[14] Jason Geng. Structured-light 3d surface imaging: atutorial. *Adv. Opt. Photon.*, 3(2):128–160, Jun 2011.

[15] Apple Inc. Face ID. https://www.apple.com/iphone-x/#face-id, 2018 (accessed May, 2018).

[16] Lothar Schermelleh, Rainer Heintzmann, and Heinrich Leonhardt. A guide to super-resolution fluorescence microscopy. *The Journal of Cell Biology*, 190(2):165–175, 2010.

[17] Rainer Heintzmann. *Structured Illumination Methods*, pages 265–279. Springer US, Boston, MA, 2006.

[18] Roland A. Terborg, Josselin Pello, Ilaria Mannelli, Juan P. Torres, and Valerio Pruneri. Ultrasensitive interferometric on-chip microscopy of transparent objects. *Science Advances*, 2(6), 2016.

[19] B. E. A. Saleh and M. C. Teich. *Fundamentals of Photonics*. John Wiley & Sons, Inc., 2001.

[20] M. Françon and S. Mallick. *Polarization interferometers: applications in microscopy and macroscopy.* Wiley series in pure and applied optics. Wiley-Interscience, 1971.

[21] Chunmin Zhang, Jianke Zhao, and Yao Sun. Influences of the thickness, misalignment, and dispersion of the savart polariscope on the optical path difference and spectral resolution in the polarization interference imaging spectrometer. *Appl. Opt.*, 50(20):3497–3504, Jul 2011.

[22] Xun Hou Jie Li, Jingping Zhu. Comment on the paper design and analysis of wide-field-of-view polarization imaging spectrometer. *Optical Engineering*, 50:50 – 50 – 2, 2011.

[23] Tingkui Mu Chunmin Zhang. Response to the comment on design and analysis of wide-field-of-view polarization imaging spectrometer. *Optical Engineering*, 50:50 – 50 – 3, 2011.

[24] Maximino Avenda no Alejo and Martha Rosete-Aguilar. Optical path difference in a plane-parallel uniaxial plate. *J. Opt. Soc. Am. A*, 23(4):926–932, Apr 2006.

[25] E Abramochkin and V Volostnikov. Spiral-type beams. *Optics Communications*, 102(3-4):336–350, 1993.

[26] Evgenii Grigor'evich Abramochkin and Vladimir Gennadievich Volostnikov. Spiral light beams. *Physics-Uspekhi*, 47(12):1177–1203, 2004.

[27] J. Durnin, J. J. Miceli, and J. H. Eberly. Diffraction-free beams. *Physical Review Letters*, 58(15):1499–1501, 1987.

[28] D. McGloin and K. Dholakia. Bessel beams: Diffraction in a new light. *Contemporary Physics*, 46(1):15–28, Jan 2005.

[29] Carlos López-Mariscal, Miguel A. Bandres, and Julio Gutiérrez-Vega. Observation of the experimental propagation properties of helmholtz-gauss beams. *Optical Engineering*, 45(6):068001, 2006.

[30] I. Ricardez-Vargas and K. Volke-Sepúlveda. Experimental generation and dynamical reconfiguration of different circular optical lattices for applications in atom trapping. *Journal of the Optical Society of America B*, 27(5):948, Apr 2010.

[31] R. J. Hernández-Hernández, R. A. Terborg, I. Ricardez-Vargas, and K. Volke-Sepúlveda. Experimental generation of mathieu–gauss beams with a phase-only spatial light modulator. *Appl. Opt.*, 49(36):6903–6909, Dec 2010.

[32] David J. Cuccia, Frederic Bevilacqua, Anthony J. Durkin, and Bruce J. Tromberg. Modulated imaging: quantitative analysis and tomography of turbid media in the spatial-frequency domain. *Opt. Lett.*, 30(11):1354–1356, Jun 2005.

[33] Bruce J. Tromberg David J. Cuccia Thomas D. O'Sullivan, Albert E. Cerussi. Diffuse optical imaging using spatially and temporally modulated light. *Journal of Biomedical Optics*, 17:17 – 17 – 15, 2012.

[34] Roshita D. Ramkhalawon, Thomas G. Brown, and Miguel A. Alonso. Imaging the polarization of a light field. *Opt. Express*, 21(4):4106–4115, Feb 2013.

[35] Brandon G. Zimmerman and Thomas G. Brown. Star test image-sampling polarimeter. *Opt. Express*, 24(20):23154–23161, Oct 2016.

[36] D. Gabor. Microscopy by reconstructed wave-fronts. *Proceedings of the Royal Society of London A: Mathematical, Physical and Engineering Sciences*, 197(1051):454–487, 1949.

[37] Raoul F Vanligten and Harold Osterberg. Holographic microscopy. *Nature*, 211(5046):282–283, Jul 1966.

[38] Tong Zhang and Ichirou Yamaguchi. Three-dimensional microscopy with phase-shifting digital holography. *Opt. Lett.*, 23(15):1221–1223, Aug 1998.

[39] F. Zernike. Phase contrast, a new method for the microscopic observation of transparent objects. *Physica*, 9(7):686–698, Jul 1942.

[40] Severin Fürhapter, Alexander Jesacher, Stefan Bernet, and Monika Ritsch-Marte. Spiral phase contrast imaging in microscopy. *Opt. Express*, 13(3):689–694, Feb 2005.

[41] R. D. Allen, G. B. David, and G. Nomarski. The zeiss-Nomarski differential interference equipment for transmitted-light microscopy. *Zeitschrift Für Wissenschaftliche Mikroskopie Und Mikroskopische Technik*, 69(4):193–221, Nov 1969.

[42] Jaime Ortega-Arroyo and Philipp Kukura. Interferometric scattering microscopy (iscat): new frontiers in ultrafast and ultrasensitive optical microscopy. *Physical Chemistry Chemical Physics*, 14(45):15625–15636, 2012.

[43] Matz Liebel, James T Hugall, and Niek F van Hulst. Ultrasensitive label-free nanosensing and high-speed tracking of single proteins. *Nano letters*, 17(2):1277–1281, 2017.

[44] L. Repetto, E. Piano, and C. Pontiggia. Lensless digital holographic microscope with light-emitting diode illumination. *Opt. Lett.*, 29(10):1132–1134, May 2004.

[45] Xiquan Cui, Lap Man Lee, Xin Heng, Weiwei Zhong, Paul W. Sternberg, Demetri Psaltis, and Changhuei Yang. Lensless high-resolution on-chip optofluidic microscopes for caenorhabditis elegans and cell imaging. *Proceedings of the National Academy of Sciences*, 105(31):10670–10675, 2008.

[46] Onur Mudanyali, Waheb Bishara, and Aydogan Ozcan. Lensfree super-resolution holographic microscopy using wetting films on a chip. *Opt. Express*, 19(18):17378–17389, Aug 2011.

[47] Najva Akbari Alon Greenbaum, Alborz Feizi and Aydogan Ozcan. Wide-field computational color imaging using pixel super-resolved on-chip microscopy. *Opt. Express*, 21(10):12469–12483, May 2013.

[48] Chulwoo Oh, Serhan O. Isikman, Bahar Khademhosseinieh, and Aydogan Ozcan. On-chip differential interference contrast microscopy using lensless digital holography. *Opt. Express*, 18(5):4717–4726, Mar 2010.

[49] J. M. Prez, M. Jofre, P. Martnez, M. A. Yez, V. Catalan, and V. Pruneri. An image cytometer based on angular spatial frequency processing and its validation for rapid detection and quantification of waterborne microorganisms. *The Analyst*, 140(22):7734–7741, 2015.

[50] DaeCheol Lim and Dae-Hwa Jeong. Zone-based inspection and defect classification for lcd manufacturing: Trivial defect free procedure for tft glass inspection. *International Journal of Optomechatronics*, 1(3):312–330, 2007.

[51] Hirofumi Minami, Junichi Mori, Susumu Iwai, Hideki Moriya, and Naruo Watanabe. Manufacturing and inspection equipment for efficient production of large lcds. *Hitachi Rev*, 60(5):228–232, 2011.

[52] Gavin MacBeath. Protein microarrays and proteomics. *Nature genetics*, 32:526, 2002.

[53] Richard B Jones, Andrew Gordus, Jordan A Krall, and Gavin MacBeath. A quantitative protein interaction network for the erbb receptors using protein microarrays. *Nature*, 439(7073):168, 2006.

[54] Karen S Anderson, Sahar Sibani, Garrick Wallstrom, Ji Qiu, Eliseo A Mendoza, Jacob Raphael, Eugenie Hainsworth, Wagner R Montor, Jessica Wong, Jin G Park, et al. Protein microarray signature of autoantibody biomarkers for the early detection of breast cancer. *Journal of proteome research*, 10(1):85–96, 2010.

[55] Xiaobo Yu and Joshua LaBaer. High-throughput identification of proteins with ampylation using self-assembled human protein (nappa) microarrays. *Nature protocols*, 10(5):756, 2015.

[56] Ichirou Yamaguchi and Tong Zhang. Phase-shifting digital holography. *Optics Letters*, 22(16):1268, Aug 1997.

[57] Daniel Malacara. *Optical shop testing*, volume 59. John Wiley & Sons, 2007.

[58] J. Goodman. *Introduction to Fourier Optics*. McGraw-Hill, 2nd edition, 1996.

[59] Pasquale Memmolo, Lisa Miccio, Melania Paturzo, Giuseppe Di Caprio, Giuseppe Coppola, Paolo A Netti, and Pietro Ferraro. Recent advances in holographic 3d particle tracking. *Advances in Optics and Photonics*, 7(4):713–755, 2015.

[60] Timothy J. Holmes and Walter J. Levy. Signal-processing characteristics of differential-interference-contrast microscopy. *Appl. Opt.*, 26(18):3929–3939, Sep 1987.

[61] RM Waxler and GW Cleek. Refractive indices of fused silica at low temperatures.

[62] Yoonkey Nam, Darren W Branch, and Bruce C Wheeler. Epoxy-silane linking of biomolecules is simple and effective for patterning neuronal cultures. *Biosensors and bioelectronics*, 22(5):589–597, 2006.

[63] Kevin R King, Luanda P Grazette, Dina N Paltoo, John T McDevitt, Samuel K Sia, Paddy M Barrett, Fred S Apple, Paul A Gurbel, Ralph Weissleder, Hilary Leeds, et al. Point-of-care technologies for precision cardiovascular care and clinical research: National heart, lung, and blood institute working group. *JACC: Basic to Translational Science*, 1(1-2):73–86, 2016.

[64] Blanca Chocarro-Ruiz, Adrián Fernández-Gavela, Sonia Herranz, and Laura M Lechuga. Nanophotonic label-free biosensors for environmental monitoring. *Current opinion in biotechnology*, 45:175–183, 2017.

[65] Gerardo A Lopez, M-Carmen Estevez, Maria Soler, and Laura M Lechuga. Recent advances in nanoplasmonic biosensors: Applications and lab-on-a-chip integration. *Nanophotonics*, 6(1):123–136, 2017.

[66] Jeffrey N Anker, W Paige Hall, Olga Lyandres, Nilam C Shah, Jing Zhao, and Richard P Van Duyne. Biosensing with plasmonic nanosensors. *Nature Materials*, 7(6):442–453, 2008.

[67] Kandammathe Valiyaveedu Sreekanth, Yunus Alapan, Mohamed ElKabbash, Efe Ilker, Michael Hinczewski, Umut A Gurkan, Antonio De Luca, and Giuseppe Strangi. Extreme sensitivity biosensing platform based on hyperbolic metamaterials. *Nature materials*, 15(6):621, 2016.

[68] Enzo Di Fabrizio, Sebastian Schlücker, Jérôme Wenger, Raju Regmi, Hervé Rigneault, Giuseppe Calafiore, Melanie West, Stefano Cabrini, Monika Fleischer, Niek F van Hulst, Maria F Garcia-Parajo, Annemarie Pucci, Dan Cojoc, Charlotte A E Hauser, and Ming Ni. Roadmap on biosensing and photonics with advanced nano-optical methods. *Journal of Optics*, 18(6):063003, 2016.

[69] Alexandre G Brolo. Plasmonics for future biosensors. *Nature Photonics*, 6(11):709, 2012.

[70] Nathan C Lindquist, Prashant Nagpal, Kevin M McPeak, David J Norris, and Sang-Hyun Oh. Engineering metallic nanostructures for plasmonics and nanophotonics. *Reports on Progress in Physics*, 75(3):036501, 2012.

[71] Alessia Pallaoro, Mehran R Hoonejani, Gary B Braun, Carl D Meinhart, and Martin Moskovits. Rapid identification by surface-enhanced raman spectroscopy of cancer cells at low concentrations flowing in a microfluidic channel. *Acs Nano*, 9(4):4328–4336, 2015.

[72] Yongkang Gao, Qiaoqiang Gan, and Filbert J Bartoli. Breakthroughs in photonics 2013: research highlights on biosensors based on plasmonic nanostructures. *IEEE Photonics Journal*, 6(2):1–5, 2014.

[73] Barbora Špačková, Piotr Wrobel, Markéta Bocková, and Jiří Homola. Optical biosensors based on plasmonic nanostructures: a review. *Proceedings of the IEEE*, 104(12):2380–2408, 2016.

[74] Joshua A Jackman, Abdul Rahim Ferhan, and Nam-Joon Cho. Nanoplasmonic sensors for biointerfacial science. *Chemical Society Reviews*, 46(12):3615–3660, 2017.

[75] Jiří Homola. Surface plasmon resonance sensors for detection of chemical and biological species. *Chemical reviews*, 108(2):462–493, 2008.

[76] Francesco Mazzotta, Timothy W Johnson, Andreas B Dahlin, Jonah Shaver, Sang-Hyun Oh, and Fredrik Hook. Influence of the evanescent field decay length on the sensitivity of plasmonic nanodisks and nanoholes. *Acs Photonics*, 2(2):256–262, 2015.

[77] Sarah Unser, Ian Bruzas, Jie He, and Laura Sagle. Localized surface plasmon resonance biosensing: current challenges and approaches. *Sensors*, 15(7):15684–15716, 2015.

[78] Maria Soler, Alexander Belushkin, Andrea Cavallini, Carole Kebbi-Beghdadi, Gilbert Greub, and Hatice Altug. Multiplexed nanoplasmonic biosensor for one-step simultaneous detection of chlamydia trachomatis and neisseria gonorrhoeae in urine. *Biosensors and Bioelectronics*, 94:560–567, 2017.

[79] Ahmet A Yanik, Min Huang, Osami Kamohara, Alp Artar, Thomas W Geisbert, John H Connor, and Hatice Altug. An optofluidic nanoplasmonic biosensor for direct detection of live viruses from biological media. *Nano letters*, 10(12):4962–4969, 2010.

[80] Hyungsoon Im, Huilin Shao, Yong Il Park, Vanessa M Peterson, Cesar M Castro, Ralph Weissleder, and Hakho Lee. Label-free detection and molecular profiling of exosomes with a nano-plasmonic sensor. *Nature biotechnology*, 32(5):490, 2014.

[81] Ahmet A Yanik, Arif E Cetin, Min Huang, Alp Artar, S Hossein Mousavi, Alexander Khanikaev, John H Connor, Gennady Shvets, and Hatice Altug. Seeing protein monolayers with naked eye through plasmonic fano resonances. *Proceedings of the National Academy of Sciences*, 108(29):11784–11789, 2011.

[82] Yun Liu, Qiang Liu, Shimeng Chen, Fang Cheng, Hanqi Wang, and Wei Peng. Surface plasmon resonance biosensor based on smart phone platforms. *Scientific reports*, 5:12864, 2015.

[83] Dustin Gallegos, Kenneth D Long, Hojeong Yu, Peter P Clark, Yixiao Lin, Sherine George, Pabitra Nath, and Brian T Cunningham. Label-free biodetection using a smartphone. *Lab on a Chip*, 13(11):2124–2132, 2013.

[84] L Kwon, KD Long, Y Wan, H Yu, and BT Cunningham. Medical diagnostics with mobile devices: Comparison of intrinsic and extrinsic sensing. *Biotechnology advances*, 34(3):291–304, 2016.

[85] Aydogan Ozcan. Mobile phones democratize and cultivate next-generation imaging, diagnostics and measurement tools. *Lab on a Chip*, 14(17):3187–3194, 2014.

[86] Andrei Viktorovich Kabashin and Petr Ivanovich Nikitin. Interferometer based on a surface-plasmon resonance for sensor applications. *Quantum Electronics*, 27(7):653, 1997.

[87] F Abeles. Surface electromagnetic waves ellipsometry. *Surface Science*, 56:237–251, 1976.

[88] YH Huang, Ho Pui Ho, Siu Kai Kong, and Andrei V Kabashin. Phase-sensitive surface plasmon resonance biosensors: methodology, instrumentation and applications. *Annalen Der Physik*, 524(11):637–662, 2012.

[89] Andrei V Kabashin, Sergiy Patskovsky, and Alexander N Grigorenko. Phase and amplitude sensitivities in surface plasmon resonance bio and chemical sensing. *Optics Express*, 17(23):21191–21204, 2009.

[90] VG Kravets, F Schedin, R Jalil, L Britnell, RV Gorbachev, D Ansell, B Thackray, KS Novoselov, AK Geim, Andrei V Kabashin, et al. Singular phase nano-optics in plasmonic metamaterials for label-free single-molecule detection. *Nature materials*, 12(4):304, 2013.

[91] Juliane Junesch and Takumi Sannomiya. Reflection phase and amplitude determination of short-range ordered plasmonic nanohole arrays. *The journal of physical chemistry letters*, 5(1):247–252, 2013.

[92] Mikael Svedendahl, Ruggero Verre, and Mikael Käll. Refractometric biosensing based on optical phase flips in sparse and short-range-ordered nanoplasmonic layers. *Light: Science & Applications*, 3(11):e220, 2014.

[93] Thomas W Ebbesen, HJ Lezec, HF Ghaemi, Tineke Thio, and PA Wolff. Extraordinary optical transmission through sub-wavelength hole arrays. *Nature*, 391(6668):667, 1998.

[94] Filiz Yesilkoy, Roland A. Terborg, Josselin Pello, Alexander A. Belushkin, Yasaman Jahani, Valerio Pruneri, and Hatice Altug. Phase-sensitive plasmonic biosensor using a portable and large field-of-view interferometric microarray imager. *Light: Science & Applications*, 7(2):17152, feb 2018.

[95] C Genet and TW Ebbesen. Light in tiny holes. In *Nanoscience And Technology: A Collection of Reviews from Nature Journals*, pages 205–212. World Scientific, 2010.

[96] Arif E Cetin, Dordaneh Etezadi, Betty C Galarreta, Mickael P Busson, Yasa Eksioglu, and Hatice Altug. Plasmonic nanohole arrays on a robust hybrid substrate for highly sensitive label-free biosensing. *ACS Photonics*, 2(8):1167–1174, 2015.

[97] SL Wong and HC Ong. Phase difference mapping of two-dimensional metallic nanohole arrays. *Applied Physics Letters*, 100(23):233102, 2012.

[98] Arif E Cetin, Ahmet F Coskun, Betty C Galarreta, Min Huang, David Herman, Aydogan Ozcan, and Hatice Altug. Handheld high-throughput plasmonic biosensor using computational on-chip imaging. *Light: Science & Applications*, 3(1):e122, 2014.

[99] Lukas Novotny and Bert Hecht. *Principles of nano-optics*. Cambridge university press, 2012.

[100] Mikael Svedendahl, Si Chen, Alexandre Dmitriev, and Mikael Kall. Refractometric sensing using propagating versus localized surface plasmons: a direct comparison. *Nano letters*, 9(12):4428–4433, 2009.

[101] Rebecca L Rich and David G Myszka. Advances in surface plasmon resonance biosensor analysis. *Current opinion in biotechnology*, 11(1):54–61, 2000.

[102] Chen Situ, Mark H Mooney, Christopher T Elliott, and Jos Buijs. Advances in surface plasmon resonance biosensor technology towards high-throughput, food-safety analysis. *TrAC Trends in Analytical Chemistry*, 29(11):1305–1315, 2010.

[103] Jiří Homola. Present and future of surface plasmon resonance biosensors. *Analytical and bioanalytical chemistry*, 377(3):528–539, 2003.

[104] Hana Šípová and Jiří Homola. Surface plasmon resonance sensing of nucleic acids: a review. *Analytica chimica acta*, 773:9–23, 2013.

[105] V Shpacovitch. Application of surface plasmon resonance (spr) for the detection of single viruses and single biological nano-objects. *J. Bacteriol. Parasitol*, 3(7):e110, 2012.

[106] YH Huang, Ho Pui Ho, Siu Kai Kong, and Andrei V Kabashin. Phase-sensitive surface plasmon resonance biosensors: methodology, instrumentation and applications. *Annalen Der Physik*, 524(11):637–662, 2012.

[107] Simona Scarano, Cosimo Scuffi, Marco Mascini, and Maria Minunni. Surface plasmon resonance imaging (SPRi)-based sensing: A new approach in signal sampling and management. *Biosensors and Bioelectronics*, 26(4):1380–1385, 2010.

[108] Seyed Hashem Aref. SPR phase sensitivity enhancement in common-path polarization heterodyne interferometer by polarization tuning. *Optik-International Journal for Light and Electron Optics*, 156:619–627, 2018.

[109] LF Hoyt. New table of the refractive index of pure glycerol at 20c. *Industrial & Engineering Chemistry*, 26(3):329–332, 1934.

[110] Masahiko Daimon and Akira Masumura. Measurement of the refractive index of distilled water from the near-infrared region to the ultraviolet region. *Applied optics*, 46(18):3811–3820, 2007.

[111] RV Khrystosenko. Optimization of the surface plasmon resonance minimum detection algorithm for improvement of method sensitivity. *Semiconductor Physics Quantum Electronics & Optoelectronics*, 2015.

Symbols and abbreviations

- λ: wavelength

- ISA: Image sensor array

- LED: Light-emiting diode

- SP: Savart plate

- S: Shear distance

- LIM: Lens-free interferometric microscope

- OPD: Optical path difference

- SPR: Surface plasmon resonance

- LSPR: Localized surface plasmon resonance

- Au: Gold

- Au-NHA: Gold nano-hole arrays

- SiO_2: Silica (silicon dioxide)

- POC: Point-of-care

- FOV: Field of view

- DOF: Depth of field

- EOT: Extraordinary transmission